International Journal of Mechanical Sciences 296 (2025) 110312

Contents lists available at ScienceDirect

International Journal of Mechanical Sciences

journal homepage: www.elsevier.com/locate/ijmecsci

# Broadband and tunable vibration suppression via Piezoelectric-ABH meta-beam

Jiazhen Zhang [a], Guobiao Hu [b,*], Hao Tang [b], Yaowen Yang [a,*]

[a] School of Civil and Environmental Engineering, Nanyang Technological University, Nanyang Avenue 639798, Singapore
[b] Internet of Things Thrust, The Hong Kong University of Science and Technology (Guangzhou), Guangzhou 511400, PR China

ARTICLE INFO

*Keywords:*
Piezoelectric metamaterial
Acoustic black hole
Vibration suppression
Band gap
Riccati transfer matrix method

ABSTRACT

Piezoelectric materials and acoustic black hole (ABH) effects have been individually studied for vibration suppression, yet their combined potential in metamaterial design remains largely unexplored. This study introduces a novel metamaterial beam (meta-beam) that integrates both mechanisms: a double-leaf ABH configuration for broadband vibration suppression and tunable piezoelectric shunting circuits for adaptive resonance control. To overcome the inherent computational limitations of conventional transfer matrix methods in transmittance prediction, a Riccati transfer matrix method (RTMM) is developed to significantly enhance computational stability. Theoretical predictions are rigorously validated against finite element (FE) simulations and experimental results. The proposed meta-beam achieves a 283.5 % and 34.2 % wider total band gap range compared to conventional piezoelectric and ABH meta-beam designs, respectively. A comparative analysis highlights the influence of ABH indentation thickness profiles on band gap formation, interpreted from an energy perspective. In addition, the tunability of the meta-beam is explored by adjusting the shunt circuit inductance, facilitating the merging of local resonant and Bragg scattering band gaps into a unified one. These findings demonstrate the synergistic potential of piezoelectric-ABH integration in developing high-performance metamaterials with enhanced and customizable vibration control.

## 1. Introduction

Metamaterials with unique characteristics, particularly those leveraging the band gap phenomenon to suppress acoustic or elastic waves [1–4], have garnered significant research interest. From the perspective of the formation mechanism, band gaps can be categorized into local resonant (LR) [5,6] and Bragg scattering (BS) types [7,8]. Early studies employed mechanical oscillators to generate LR band gaps [9–11]. However, those systems suffered from limited tunability and bulky sizes, hindering practical implementation. To address above challenges, piezoelectric metamaterials with inductive or capacitive shunt circuits were proposed, leveraging electromechanical coupling effects. Utilizing these effects, piezoelectric transducers, easily attached to the target structure, can generate LC resonance and controllable band gaps, capitalizing on the high transformability of the shunting circuit. Pioneering work by Thorp et al., [12] periodically placed shunted piezoelectric patches along rods to control the longitudinal wave propagation. Following the same idea, piezoelectric metamaterials found extensive application in the vibration suppression of plates [13–16] and beams [17–20]. Additionally, negative capacitances [21–23] and nonlinear shunt circuits [24–26] were employed to enlarge the bandwidth of band gaps. However, physically connected periodic arrangement designs for piezoelectric metamaterial beams (meta-beams) are impractical due to the challenges in ensuring electrical insulation between neighboring unit cells, not to mention the difficulty in implementing the electrodes. Consequently, stepped configurations were proposed [27–29], where only half of the unit cell was covered by a piezoelectric patch, leaving the other half free for electrode installation.

Unlike piezoelectric metamaterials relying solely on electromechanical coupling, acoustic black hole (ABH) structures exploit geometric tailoring for vibration suppression. ABH structures, characterized by a thickness gradually approaching zero according to a power law, can effectively manipulate and reflect flexural waves [30]. Pekeris [31] first discovered the phenomenon of sound velocity decreasing to zero as it travels through a non-uniform stratified fluid. Subsequently, Mironov [32] proposed the concept of ABH and applied it to the vibration suppression of plates. Various structures with ABH indentations have been proposed, including single-leaf beams [33,34], double-leaf beams [35,

* Corresponding authors.
*E-mail addresses:* guobiaohu@hkust-gz.edu.cn (G. Hu), cywyang@ntu.edu.sg (Y. Yang).

https://doi.org/10.1016/j.ijmecsci.2025.110312
Received 27 February 2025; Received in revised form 9 April 2025; Accepted 26 April 2025
Available online 28 April 2025

36], V-shaped beams [37], and pillars [38,39]. Notably, double-leaf ABH beams have been shown to generate a wider first band gap by incorporating both LR and BS effects [40]. Techniques such as graded strategies [15,20,34] and the use of dynamic vibration absorbers [41] have been employed to broaden the widths of band gaps in ABH structures. However, it is important to note that ABH effects primarily occur above a characteristic frequency where the wavelength becomes smaller than the ABH feature size. This threshold frequency, known as the cut-on frequency, serves as a key indicator for evaluating the effective operational range of a single ABH segment [42]. Recent advances incorporating metamaterial concepts have demonstrated that ABH meta-beams can achieve wide band gaps and effective wave suppression even below this cut-on frequency [43,44]. Nevertheless, a significant challenge remains in enhancing the tunability of ABH structures without requiring complex geometric modifications.

Theoretical methods play a crucial role in investigating band gaps and wave propagation in metamaterials. Various methods, including the spectral element method (SEM), plane wave expansion (PWE) method, and Rayleigh-Ritz method (RRM), have been developed and widely employed for band gap analysis. Among them, the transfer matrix method (TMM), originally developed by Targoff [45], remains one of the most prevalent approaches, particularly for metamaterials modeled using Euler-Bernoulli or Timoshenko beam theory. Compared to SEM [46–48], which offers high accuracy at the expense of significant computational cost, TMM provides a balance between efficiency and analytical tractability. Unlike PWE [49,50], which is well-suited for infinite periodic structures but less effective for finite systems, TMM excels in calculating the transmittance of finitely long systems with a limited number of unit cells. Additionally, while RRM [35,51] is effective in capturing eigenmodes of low degree-of-freedom systems, it lacks the versatility and flexibility for analyzing complex metamaterial architectures. Overall, TMM is distinguished by its relatively high computational efficiency and the notable advantage that it does not require derivation of the global dynamic equations of the system. After discretizing the beam into segments, TMM is applied to both single-leaf [41,52] and double-leaf [53] ABH structures by assembling the transfer matrix of each segment based on Euler-Bernoulli beam theory. TMM has also proven to be efficient in band gap prediction for piezoelectric metamaterials [12,54]. However, a recent study by Hu *et al.*, [28] pointed out that applying conventional TMM to a piezoelectric coupling system leads to a collapse in transmittance calculations in the high-frequency domain. This collapse is caused by numerical instability due to the successive multiplication of transfer matrices. To improve the accuracy and stability, the Riccati transfer matrix method (RTMM), first proposed by Horner *et al.*, [55], offers an effective solution. RTMM combines the Riccati transformation with TMM to reduce the matrix magnitude, thereby providing stable calculation results. RTMM has been widely applied to model chain systems [56,57], single-leaf ABH beams [53,58], and multibody systems with closed loops [59], demonstrating high accuracy and stability across a range of problems.

Recent research has explored the application of piezoelectric transducers on ABH structures. Deng *et al.*, [60] attached piezoelectric layers to an ABH bimorph cantilever for energy harvesting and developed a semi-analytical model for simulation. Building on this, Li *et al.*, [61] utilized resistive and inductive shunt circuits on a similar bimorph cantilever to enhance energy harvesting efficiency. While piezoelectric ABH structures have been widely explored for energy harvesting [62–64], their integration has also shown significant promise for vibration suppression [65]. Conventional approaches typically attach piezoelectric patches to ABH structures to reduce vibrations via shunt damping techniques [66–70]. For instance, Wan et al., [71] enhanced the vibration suppression performance of ABH plates below the cut-on frequency using piezoelectric shunt damping, while Wang et al., [72] employed passive strategies with piezoelectric elements to exploit the ABH effect for absorbing medium to high-frequency waves through localized damping. Further advancements introduced electrical nonlinearity to standalone ABH beams, improving tunability in vibration suppression [73] and enhancing low-frequency performance [74]. However, these studies primarily focus on shunt damping applications in standalone ABH structures, with limited exploration of piezoelectric-ABH coupling in metamaterial beam designs, particularly concerning hybrid band gap formation and merging. A notable exception is Chen et al., [75], who combined piezoelectric metamaterials with a single-leaf ABH structure, though their work lacked experimental validation. More recently, Wu et al., [76] proposed a similar meta-beam but emphasized machine learning-based optimization of the vibration suppression region. Compared to those single-leaf configurations, the double-leaf ABH structure offers a broader first band gap, presenting a key advantage. To address these research gaps, this study introduces a novel piezoelectric meta-beam with a double-leaf ABH configuration, employing RTMM for precise transmittance prediction and investigating the synergistic effects of piezoelectric and ABH induced band gaps for broadband vibration suppression.

This paper is structured into five sections. Following the brief introduction in the first section, Section 2 presents a theoretic analysis of the proposed meta-beam based on the Timoshenko beam theory, where the band structure and transmittance response are predicted. Section 3 provides validation through the finite element (FE) simulation and experiments, along with an investigation of band gap tunability, including discussions on the dependence of geometric and electric parameters. Finally, Section 4 summarizes the key findings and highlights the merits of the proposed meta-beam.

## 2. Theoretical modelling using Riccati transfer matrix method

This section provides a comprehensive overview of the structural design and theoretical model of the piezoelectric meta-beam with the double-leaf ABH configuration. First, a graphical representation illustrates the geometric design of the proposed meta-beam. Subsequently, the governing equations are derived using the Timoshenko beam theory. The band structure is calculated using the TMM and Bloch's theorem, and transmittance is predicted by RTMM.

Fig. 1 illustrates the piezoelectric meta-beam with the double-leaf ABH configuration. In the local coordinate system, the $x$-axis is along the length direction, and the y-axis is the width direction. Within a unit cell, the double-leaf ABH beam has a length of $L_{\mathrm{ABH}}$, with an indentation length of $L_t$, and the piezoelectric-covered beam has a length of $L_p$. The thicknesses of the substrate and piezoelectric patches are, respectively, $h_s$ and $h_p$. The thickness of the ABH indentation $h_t$ is governed by the ABH profile, $h_t(x) = h_s - 2(\varepsilon x^m + h_0)$, where $\varepsilon$ and $m$ represent the smoothness coefficient and the power order, respectively. $h_0$ denotes the thinnest thickness of the substrate. It is worth mentioning that $m$ should be greater than or equal to 2. Additionally, the widths of all the beams are identically equal to $b$.

As depicted in Fig. 2(a), the top and bottom piezoelectric layers in each unit cell are connected in parallel and shunted to an external inductance circuit, with the inductance of $L_d$. Fig. 2(b) shows the equivalent circuit of a single segment of the piezoelectric beam, with $C_p$ representing the internal capacitance of the in-parallel connected piezoelectric layers.

### 2.1. Governing equations

As introduced in Section 1, previous studies of tapered ABH segments typically simplify them as stepped Euler-Bernoulli beams composed of multiple segments with constant thickness. However, after discretization, these stepped beams no longer satisfy the slender beam assumption for Euler-Bernoulli beams. To address this issue, this paper employs Timoshenko beam theory to improve modelling fidelity and predictive capabilities.

According to the prevailing norm on piezoelectricity, the coupling between the elastic and electrostatic properties of piezoelectric patches

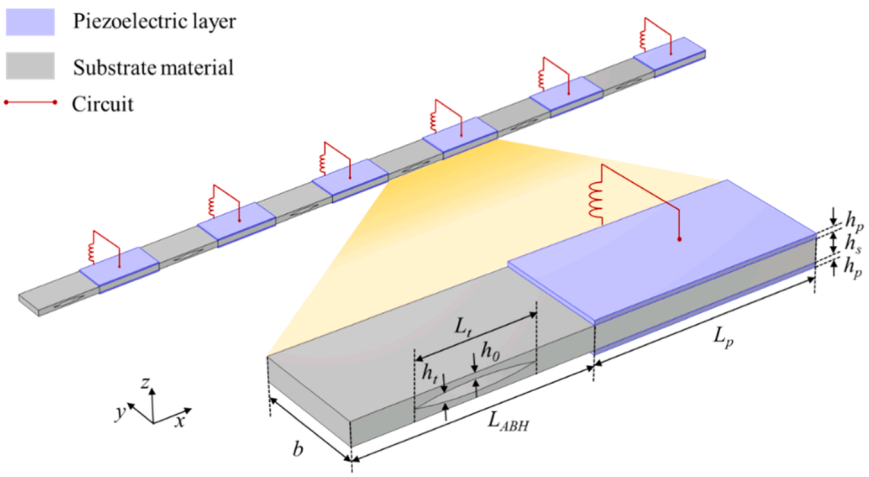


**Fig. 1.** Proposed piezoelectric meta-beam with double-leaf ABH configuration.

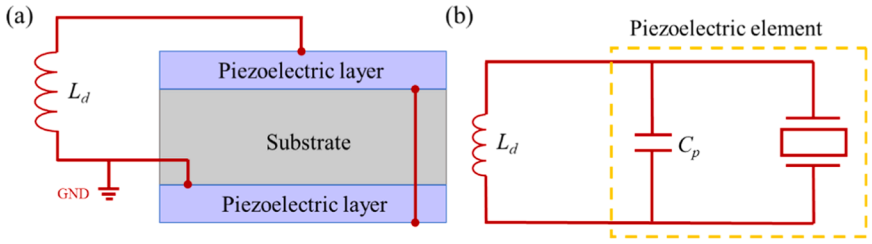


**Fig. 2.** Schematic of circuit connections. (a) Close-up view of shunt circuit connection, and (b) equivalent circuit of piezoelectric beam.

can be expressed as follows:

$$\begin{bmatrix} \varepsilon_p \\ \gamma_p \\ D_3 \end{bmatrix} = \begin{bmatrix} S_{11}^E & 0 & d_{31} \\ 0 & S_{55}^E & 0 \\ d_{31} & 0 & \varepsilon_{33}^T \end{bmatrix} \begin{bmatrix} \sigma_p \\ \tau_p \\ E_3 \end{bmatrix}, \tag{1}$$

where $\varepsilon_p$ and $\gamma_p$ represent the longitudinal and shear strain along the beam's length and thickness directions, respectively. Correspondingly, $\sigma_p$ and $\tau_p$ are the longitudinal and shear stresses. $D_3$ is the electric displacement, and $E_3$ is the dielectric field in the thickness direction. $S_{11}^E$ and $S_{55}^E$ are the elastic compliance constants. $d_{31}$ is the piezoelectric constant. The stresses can also be expressed in terms of strains:

$$\begin{bmatrix} \sigma_p \\ \tau_p \\ E_3 \end{bmatrix} = \begin{bmatrix} C_{11}^D & 0 & -h_{31} \\ 0 & C_{55}^D & 0 \\ -h_{31} & 0 & \beta_{33}^S \end{bmatrix} \begin{bmatrix} \varepsilon_p \\ \gamma_p \\ D_3 \end{bmatrix}, \tag{2}$$

where $C_{11}^D$ and $C_{55}^D$ are elastic stiffness constants. $\beta_{33}^S$ is the permittivity constant, and $h_{31}$ is the piezoelectric constant. As the commercial FE software, COMSOL, requires piezoelectric properties to be input in stress-strain form $\{C_{11}^E, C_{55}^E, e_{31}, \varepsilon_{33}^S\}$, the relationship between the different sets of piezoelectric constants can be derived as:

$$\begin{cases} S_{11}^E = \dfrac{1}{C_{11}^E} \\ S_{55}^E = \dfrac{1}{C_{55}^E} \\ d_{31} = \dfrac{e_{31}}{C_{11}^E} \\ \varepsilon_{33}^T = \varepsilon_{33}^S + \dfrac{d_{31}^2}{S_{11}^E} \end{cases}, \begin{cases} C_{11}^D = \dfrac{\varepsilon_{33}^T}{\varepsilon_{33}^T S_{11}^E - d_{31}^2} \\ C_{55}^D = \dfrac{1}{S_{55}^E} \\ h_{31} = \dfrac{d_{31}}{\varepsilon_{33}^T S_{11}^E - d_{31}^2} \\ \beta_{33}^S = \dfrac{S_{11}^E}{S_{11}^E \varepsilon_{33}^T - d_{31}^2} \end{cases}. \tag{3}$$

Considering the small deflection assumption, the strain components in the substrate and piezoelectric material can be represented as functions of the transverse displacement $w(x, t)$ and rotational angle of the cross-section $\phi(x, t)$ at the position $x$ and time instant $t$

$$\begin{cases} \varepsilon_s = \varepsilon_p = -\dfrac{\partial \phi(x,t)}{\partial x} y \\ \gamma_s = \gamma_p = \phi(x,t) - \dfrac{\partial w(x,t)}{\partial x}. \end{cases} \tag{4}$$

Considering the Young's modules $E_s$ and shear modules $G_s$ of the substrate, the relationship between stresses and strains in the substrate and piezoelectric patches can be expressed respectively as:

$$\begin{cases} \sigma_s = E_s \varepsilon_s \\ \tau_s = G_s \gamma_s \end{cases}, \begin{cases} \sigma_p = C_{11}^D \varepsilon_p - D_3 h_{31} \\ \tau_p = C_{55}^D \gamma_p. \end{cases} \tag{5}$$

Based on Eq. (5), the governing equations of the piezoelectric meta-beam, in terms of transverse displacement $w(x, t)$, rotation angle $\phi(x, t)$, and longitudinal displacement $u(x, t)$, can be derived by applying Hamilton's principle [28]:

$$\widehat{\rho A} \frac{\partial^2 w(x,t)}{\partial t^2} + \kappa \widehat{GA} \left[ \frac{\partial \phi(x,t)}{\partial x} - \frac{\partial^2 w(x,t)}{\partial x^2} \right] = 0, \tag{6}$$

$$D_t \frac{\partial^2 \phi(x,t)}{\partial x^2} + \kappa \widehat{GA} \left[ \frac{\partial w(x,t)}{\partial x} - \phi(x,t) \right] - \widehat{\rho I_z} \frac{\partial^2 \phi(x,t)}{\partial t^2} = 0, \tag{7}$$

$$\widehat{\rho A} \frac{\partial^2 u(x,t)}{\partial x^2} - \widehat{EA} \frac{\partial^2 u(x,t)}{\partial t^2} = 0, \tag{8}$$

where $\widehat{\rho A} = \rho_s h_s b + 2\rho_p h_p b$, $\widehat{GA} = G_s h_s b + 2C_{55}^D h_p b$, $\widehat{\rho I_z} = \rho_s I_z^s + 2\rho_p I_z^p$, $\widehat{EA} = E_s h_s b + 2C_{11}^D h_p b$ with $I_z^s$ and $I_z^p$ representing the moment inertias of the cross section area of the substrate and the piezoelectric patch respectively. Under the open-circuit condition, the following

holds: $D_t = E_s I_z^s + 2C_{11}^D I_z^p - 2h_p b h_{sp}^2 h_{31}^2/\beta_{33}^S$, in which, $h_{sp}$ is the thickness difference between the substrate and piezoelectric patch. $\kappa$ is the shear correction factor.

Assume the external shunt circuit is an inductive circuit, as shown in Fig. 2, the governing equation of the circuit can be obtained by applying Kirchhoff's law:

$$\frac{di_p(t)}{dt} = \theta\left[\frac{\partial^2\phi(L,t)}{\partial t^2} - \frac{\partial^2\phi(0,t)}{\partial t^2}\right] - C_p\frac{d^2v(t)}{dt^2} = \frac{v(t)}{L_d}, \tag{9}$$

where $i_p(t)$ represents the current, and $v(t)$ is the voltage. The equivalent capacitance $C_p$ of the in-parallel connected circuit is governed by $C_p = 2\varepsilon_{33}^S b L_p/h_p$, while the constant $\theta$ is defined as $\theta = 2bh_{sp}d_{31}/S_{11}^E$. Considering a harmonic excitation and the steady-state response, $w(x, t)$, $\phi(x, t)$, $u(x, t)$ and $v(t)$ can be expressed as a product of an amplitude function and a time function using the variable separation method, i.e., $w(x, t) = W(x)e^{i\omega t}$, $\phi(x, t) = \Phi(x)e^{i\omega t}$, $u(x, t) = U(x)e^{i\omega t}$ and $v(t) = Ve^{i\omega t}$ in which $\omega$ is the circular excitation frequency. Subsequently, the governing equations Eqs. (6)-(9) can be rewritten as:

$$\omega^2\widehat{\rho A}\,W(x) + \kappa\widehat{GA}\left[\frac{d^2W(x)}{dx^2} - \frac{d\Phi(x)}{dx}\right] = 0, \tag{10}$$

$$D_t\frac{d^2\Phi(x)}{dx^2} + \kappa\widehat{GA}\left[\frac{dW(x)}{dx} - \Phi(x)\right] + \omega^2\widehat{\rho I_z}\,\Phi(x) = 0, \tag{11}$$

$$\widehat{\rho A}\frac{\partial^2U(x)}{\partial x^2} + \widehat{EA}\,\omega^2U(x) = 0, \tag{12}$$

$$-\omega^2\theta[\Phi(L) - \Phi(0)] + \omega^2C_pV = \frac{V}{L_d}. \tag{13}$$

The general solution for the transverse amplitude $W(x)$ and rotation angle $\Phi(x)$ can be assumed as:

$$\begin{cases} W(x) = Be^{ikx} \\ \Phi(x) = rBe^{ikx}. \end{cases} \tag{14}$$

Substituting Eq. (14) back into Eqs.(10) and (11) yields an eigenvalue problem. The roots of the eigenvalue problem can be derived as:

$$\begin{cases} k_1 = -k_2 = \dfrac{k_F}{\sqrt{2}}\sqrt{\eta k_F^2 + \sqrt{\eta^2k_F^4 + 4\left(1 - \eta_1k_G^4\right)}} \\ k_3 = -k_4 = \dfrac{k_F}{\sqrt{2}}\sqrt{\eta k_F^2 - \sqrt{\eta^2k_F^4 + 4\left(1 - \eta_1k_G^4\right)}}, \end{cases} \tag{15}$$

where $k_F = \sqrt{\omega}\left(\widehat{\rho A}/D_t\right)^{0.25}$, $k_G = \sqrt{\omega}\left(\widehat{\rho A}/\kappa\widehat{GA}\right)^{0.25}$, $\eta = \widehat{\rho I}/\widehat{\rho A} + D_t/\kappa\widehat{GA}$, and $\eta_1 = \widehat{\rho I}/\widehat{\rho A}$. Subsequently, Eq. (14) can be rewritten as:

$$\begin{cases} W(x) = B_1e^{ik_1x} + B_2e^{ik_2x} + B_3e^{ik_3x} + B_4e^{ik_4x} \\ \Phi(x) = r_1B_1e^{ik_1x} + r_2B_2e^{ik_2x} + r_3B_3e^{ik_3x} + r_4B_4e^{ik_4x}, \end{cases} \tag{16}$$

where $r_n = i\left(k_n^2 - k_G^4\right)/k_n$, and $B_n$ represent the state coordinates ($n = 1, 2, \ldots, 4$). The bending moment $M(x)$ and shear force $Q(x)$ can be derived as:

$$\begin{cases} M(x) = D_t\dfrac{\partial\Phi(x)}{\partial x} \\ Q(x) = \widehat{GA}\left[\dfrac{\partial W(x)}{\partial x} - \Phi(x)\right]. \end{cases} \tag{17}$$

Besides, the longitudinal displacement and axial force can be obtained in terms of the coordinates $C_n$ ($n = 1, 2$), with $\gamma^2 = \omega^2\widehat{\rho A}/\widehat{EA}$:

$$\begin{cases} U(x) = C_1\sin(\gamma x) + C_2\cos(\gamma x) \\ N(x) = \widehat{EA}\,\gamma[C_1\cos(\gamma x) - C_2\sin(\gamma x)]. \end{cases} \tag{18}$$

Thus, the modal coordinates $S_p(x)$ containing transverse displacement, rotation angle, bending moment, shear force, longitudinal displacement, and axial force in a piezoelectric segment can be expressed in the matrix form:

$$\begin{aligned} S_p(0) &= K_p\psi_p \\ S_p(L_p) &= H_p\psi_p, \end{aligned} \tag{19}$$

where the modal coordinates $S(x) = [W(x), \Phi(x), M(x), Q(x), U(x), N(x)]^T$. $\psi_p$ represents the state coordinates of the piezoelectric segment, i.e., $\psi_p = [B_1, B_2, B_3, B_4, C_1, C_2]^T$, with

$$H_p = \begin{bmatrix} e^{ik_1L_p} & e^{ik_2L_p} & e^{ik_3L_p} & e^{ik_4L_p} & 0 & 0 \\ r_1e^{ik_1L_p} & r_2e^{ik_2L_p} & r_3e^{ik_3L_p} & r_4e^{ik_4L_p} & 0 & 0 \\ iD_tk_1r_1e^{ik_1L_p} & iD_tk_2r_2e^{ik_2L_p} & iD_tk_3r_3e^{ik_3L_p} & iD_tk_4r_4e^{ik_4L_p} & 0 & 0 \\ \widehat{GA}\,(ik_1 - r_1)e^{ik_1L_p} & \widehat{GA}\,(ik_2 - r_2)e^{ik_2L_p} & \widehat{GA}\,(ik_3 - r_3)e^{ik_3L_p} & \widehat{GA}\,(ik_4 - r_4)e^{ik_4L_p} & 0 & 0 \\ 0 & 0 & 0 & 0 & \sin(\gamma L_p) & \cos(\gamma L_p) \\ 0 & 0 & 0 & 0 & \widehat{EA}\,\gamma\cos(\gamma L_p) & -\widehat{EA}\,\gamma\sin(\gamma L_p) \end{bmatrix}$$

and

$$K_p = \begin{bmatrix} 1 & 1 & 1 & 1 & 0 & 0 \\ r_1 & r_2 & r_3 & r_4 & 0 & 0 \\ iD_tk_1r_1 & iD_tk_2r_2 & iD_tk_3r_3 & iD_tk_4r_4 & 0 & 0 \\ \widehat{GA}\,(ik_1 - r_1) & \widehat{GA}\,(ik_2 - r_2) & \widehat{GA}\,(ik_3 - r_3) & \widehat{GA}\,(ik_4 - r_4) & 0 & 0 \\ 0 & 0 & 0 & 0 & 0 & 1 \\ 0 & 0 & 0 & 0 & \widehat{EA}\,\gamma & 0 \end{bmatrix}.$$

Additionally, Eq. (13) can be reformulated with a constant $g$, which is defined as $g = L_d\omega^2\theta/(L_d\omega^2C_p - 1)$

$$V = g[\Phi(L) - \Phi(0)]. \tag{20}$$

The bending moments induced by the piezoelectric effect can be derived as:

$$M = \theta V. \tag{21}$$

Thus, combining Eqs.(20) and (21), Eq. (19) is updated with extra bending moments:

$$\begin{aligned} S_p(0) &= (K_p + G)\psi_p \\ S_p(L_p) &= (H_p + G)\psi_p. \end{aligned} \tag{22}$$

where

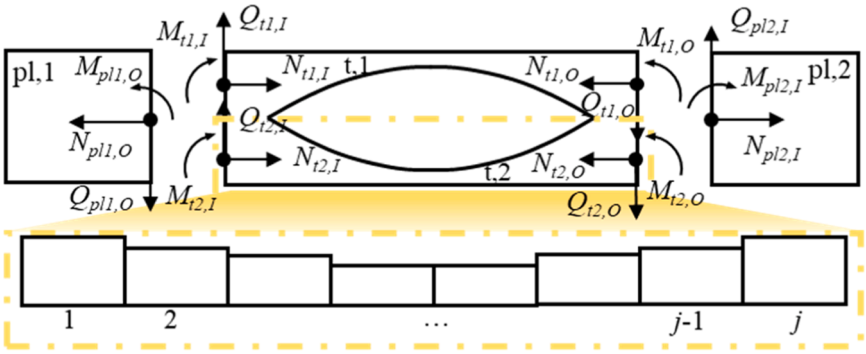


**Fig. 3.** Force analysis between plain and tapered segments with an equivalent treatment of tapered section.

$$G=\begin{bmatrix} 0 & 0 & 0 & 0 & 0 & 0 \\ 0 & 0 & 0 & 0 & 0 & 0 \\ g\theta r_1(e^{ik_1L_p}-1) & g\theta r_2(e^{ik_2L_p}-1) & g\theta r_3(e^{ik_3L_p}-1) & g\theta r_4(e^{ik_4L_p}-1) & 0 & 0 \\ 0 & 0 & 0 & 0 & 0 & 0 \\ 0 & 0 & 0 & 0 & 0 & 0 \\ 0 & 0 & 0 & 0 & 0 & 0 \end{bmatrix}.$$

Fig. 3. depicts the force analysis between segments, with the ABH segment divided into plain segments pl,1 and pl,2, and tapered segments t,1 and t,2. It is worth mentioning that the subscripts *I* and *O* indicate the input and output of a segment. Additionally, the tapered segments are treated as a combination of *j* plain segments.

Similar to Eqs.(6)-(8), the governing equations in the transverse and longitudinal direction of a plain beam member are as follows:

$$\rho_s A_i\frac{d^2w_i(x,t)}{dt^2}+\kappa G_s A_i\left[\frac{d\phi_i(x,t)}{dx}-\frac{d^2w_i(x,t)}{dx^2}\right]=0, \tag{23}$$

$$\rho_s I_i\frac{d^2\phi_i(x,t)}{dt^2}+\kappa G_s A_i\left[\phi_i(x,t)-\frac{dw_i(x,t)}{dx}\right]-E_s I_i\frac{d^2\phi_i(x,t)}{dx^2}=0, \tag{24}$$

$$\rho_s A_i\frac{\partial^2u_i(x,t)}{\partial x^2}-E_s A_i\frac{\partial^2u_i(x,t)}{\partial t^2}=0, \tag{25}$$

where $A_i$ and $I_i$ represent the cross-sectional area and moment inertia of the cross-sectional area of discrete segments, respectively. $w_i(x, t)$, $u_i(x, t)$, and $\phi_i(x, t)$ stand for the transverse and longitudinal deflections and the rotation angle of the beam cross-section. Since the solutions to Eqs. (23)-(25) resemble those of the piezoelectric segment, the derivation details are omitted. The modal coordinates of each segment can be expressed as:

$$\begin{aligned} S_i(0)&=K_i\psi_i \\ S_i(L_i)&=H_i\psi_i, \end{aligned} \tag{26}$$

where $L_i$ is the length of the discrete segment. The continuity condition between $j$th and $(j+1)$th segments in the tapered segment can be written as:

$$\begin{cases} W_j(L_i)=W_{j+1}(0) \\ \Phi_j(L_i)=\Phi_{j+1}(0) \\ M_j(L_i)=M_{j+1}(0)+d_jN_{j+1}(0) \\ Q_j(L_i)=Q_{j+1}(0) \\ U_j(L_i)=U_{j+1}(0)+d_j\Phi_{j+1}(0) \\ N_j(L_i)=N_{j+1}(0) \end{cases} \tag{27}$$

It is worth noting that the thickness difference $d_j$ between each discrete segment cannot be ignored. As a result, the contribution of axial forces to bending moment calculation should be considered to improve accuracy. Rewrite Eq. (27), and the relationship between the first and the last segment can be written in a matrix form with a local transfer matrix $T_t$:

$$\begin{cases} T_t\psi_1=\psi_j \\ T_t=K_j^{-1}H_{j-1}K_{j-1}^{-1}H_{j-2}\ldots K_2^{-1}H_1 \end{cases} \tag{28}$$

As shown in Fig. 3, the geometric relationship between the tapered segments 1 and 2 can be expressed as follows:

$$\begin{cases} W_{t1}(0)=W_{t2}(0) \\ \Phi_{t1}(0)=\Phi_{t2}(0) \\ U_{t1}(0)=U_{t2}(0)+2d\Phi_{t1}(0) \\ W_{t1}(L_t)=W_{t2}(L_t) \\ \Phi_{t1}(L_t)=\Phi_{t2}(L_t) \\ U_{t1}(L_t)=U_{t2}(L_t)+2d\Phi_{t1}(L_t), \end{cases} \tag{29}$$

where $d$ denotes the distance between the two shape centers of tapered segments 1 and 2. Reformulating Eq. (29) in a matrix form yields:

$$A\psi_{t1,1}=B\psi_{t2,1} \tag{30}$$

where $A=\begin{bmatrix} A_1 \\ A_2T_t \end{bmatrix}$, $B=\begin{bmatrix} B_1 \\ B_2T_t \end{bmatrix}$, $A_1=\begin{bmatrix} -dr_1 & -dr_2 & -dr_3 & -dr_4 & 0 & 1 \\ 1 & 1 & 1 & 1 & 0 & 0 \\ r_1 & r_2 & r_3 & r_4 & 0 & 0 \end{bmatrix}$,

$$A_2=\begin{bmatrix} -dr_1e^{ik_1L_j} & -dr_2e^{ik_2L_j} & -dr_3e^{ik_3L_j} & -dr_4e^{ik_4L_j} & \sin(\gamma L_j) & \cos(\gamma L_j) \\ e^{ik_1L_j} & e^{ik_2L_j} & e^{ik_3L_j} & e^{ik_4L_j} & 0 & 0 \\ r_1e^{ik_1L_j} & r_2e^{ik_2L_j} & r_3e^{ik_3L_j} & r_4e^{ik_4L_j} & 0 & 0 \end{bmatrix},$$

$$B_1=\begin{bmatrix} dr_1 & dr_2 & dr_3 & dr_4 & 0 & 1 \\ 1 & 1 & 1 & 1 & 0 & 0 \\ r_1 & r_2 & r_3 & r_4 & 0 & 0 \end{bmatrix},$$

and

$$B_2=\begin{bmatrix} dr_1e^{ik_1L_j} & dr_2e^{ik_2L_j} & dr_3e^{ik_3L_j} & dr_4e^{ik_4L_j} & \sin(\gamma L_j) & \cos(\gamma L_j) \\ e^{ik_1L_j} & e^{ik_2L_j} & e^{ik_3L_j} & e^{ik_4L_j} & 0 & 0 \\ r_1e^{ik_1L_j} & r_2e^{ik_2L_j} & r_3e^{ik_3L_j} & r_4e^{ik_4L_j} & 0 & 0 \end{bmatrix}.$$

Besides, $\psi_{tn,1}$ represents the state coordinates of the first segment in the tapered segments 1 and 2. In addition, the continuity condition between plain and tapered segments can be represented as:

$$\begin{cases} W_{pl,1}(L_{pl})=W_{t1}(0) \\ \Phi_{pl,1}(L_{pl})=\Phi_{t1}(0) \\ M_{pl,1}(L_{pl})=M_{t1}(0)+M_{t2}(0)+dN_{t1}(0)-dN_{t2}(0) \\ Q_{pl,1}(L_{pl})=Q_{t1}(0)+Q_{t2}(0) \\ U_{pl,1}(L_{pl})=U_{t1}(0)+d\Phi_{t1}(0) \\ N_{pl,1}(L_{pl})=N_{t1}(0)+N_{t2}(0). \end{cases} \tag{31}$$

$$\begin{cases} W_{t1}(L_t) = W_{pl,2}(0) \\ \Phi_{t1}(L_t) = \Phi_{pl,2}(0) \\ M_{t1}(L_t) + M_{t2}(L_t) + dN_{t1}(L_t) - dN_{t2}(L_t) = M_{pl,2}(0) \\ Q_{t1}(L_t) + Q_{t2}(L_t) = Q_{pl,2}(0) \\ U_{t1}(L_t) + d\Phi_{t1}(L_t) = U_{pl,2}(0) \\ N_{t1}(L_t) + N_{t2}(L_t) = N_{pl,2}(0). \end{cases} \tag{32}$$

where

$S_{pl,n}(x) = \left[W_{pl,n}(x), \Phi_{pl,n}(x), M_{pl,n}(x), Q_{pl,n}(x), U_{pl,n}(x), N_{pl,n}(x)\right]^T$ represents the modal coordinates of the plain beam segments 1 and 2 with a length of $L_{pl}$, i.e., $L_{pl} = L_{ABH}$ - $L_t$. Similarly, rearranging Eqs.(31) and (32) in the matrix form yields:

$$\begin{aligned} H_{pl,1}\psi_{pl,1} &= K_{t1}\psi_{t1,1} + K_{t2}\psi_{t2,1} \\ H_{t1}\psi_{t1,j} + H_{t2}\psi_{t2,j} &= K_{pl,2}\psi_{pl,2}, \end{aligned} \tag{33}$$

in which,

$$K_{t1} = \begin{bmatrix} 1 & 1 & 1 & 1 & 0 & 0 \\ r_1 & r_2 & r_3 & r_4 & 0 & 0 \\ iE_sI_ik_1r_1 & iE_sI_ik_2r_2 & iE_sI_ik_3r_3 & iE_sI_ik_4r_4 & dE_sA_i\gamma & 0 \\ G_sA_i(ik_1 - r_1) & G_sA_i(ik_2 - r_2) & G_sA_i(ik_3 - r_3) & G_sA_i(ik_4 - r_4) & 0 & 0 \\ -dr_1 & -dr_2 & -dr_3 & -dr_4 & 0 & 1 \\ 0 & 0 & 0 & 0 & E_sA_i\gamma & 0 \end{bmatrix},$$

$$K_{t2} = \begin{bmatrix} 0 & 0 & 0 & 0 & 0 & 0 \\ 0 & 0 & 0 & 0 & 0 & 0 \\ iE_sI_ik_1r_1 & iE_sI_ik_2r_2 & iE_sI_ik_3r_3 & iE_sI_ik_4r_4 & -dE_sA_i\gamma & 0 \\ G_sA_i(ik_1 - r_1) & G_sA_i(ik_2 - r_2) & G_sA_i(ik_3 - r_3) & G_sA_i(ik_4 - r_4) & 0 & 0 \\ 0 & 0 & 0 & 0 & 0 & 0 \\ 0 & 0 & 0 & 0 & E_sA_i\gamma & 0 \end{bmatrix},$$

$$H_{t1} = \begin{bmatrix} e^{ik_1L_i} & e^{ik_2L_i} & e^{ik_3L_i} & e^{ik_4L_i} & 0 & 0 \\ r_1e^{ik_1L_i} & r_2e^{ik_2L_i} & r_3e^{ik_3L_i} & r_4e^{ik_4L_i} & 0 & 0 \\ iE_sI_sk_1r_1e^{ik_1L_i} & iE_sI_sk_2r_2e^{ik_2L_i} & iE_sI_sk_3r_3e^{ik_3L_i} & iE_sI_sk_4r_4e^{ik_4L_i} & dE_sA_s\gamma\cos(\gamma L_i) & -dE_sA_s\gamma\sin(\gamma L_i) \\ G_sA_s(ik_1 - r_1)e^{ik_1L_i} & G_sA_s(ik_2 - r_2)e^{ik_2L_i} & G_sA_s(ik_3 - r_3)e^{ik_3L_i} & G_sA_s(ik_4 - r_4)e^{ik_4L_i} & 0 & 0 \\ -dr_1e^{ik_1L_i} & -dr_2e^{ik_2L_i} & -dr_3e^{ik_3L_i} & -dr_4e^{ik_4L_i} & \sin(\gamma L_i) & \cos(\gamma L_i) \\ 0 & 0 & 0 & 0 & E_sA_s\gamma\cos(\gamma L_i) & -E_sA_s\gamma\sin(\gamma L_i) \end{bmatrix},$$

**Table 1**
Structural parameters of proposed meta-beam.

| Geometrical Parameters | Value | Material Parameters | Value |
|---|---|---|---|
| Substrate beam length $L_{ABH}$ and $L_p$ | 0.02 m | Substrate Young's modulus $E_s$ | 100 GPa |
| ABH segment length $L_t$ | 0.01 m | Substrate shear modulus $G_s$ | 40 GPa |
| Substrate beam thickness $h_s$ | 0.002 m | Substrate density $\rho_s$ | 7165 kg/m$^3$ |
| Piezoelectric patch thickness $h_p$ | 0.0004 m | Piezo layer Young's modulus ${C_{11}}^E$ | 66 GPa |
| Beam width $b$ | 0.02 m | Piezo layer shear modulus ${C_{55}}^S$ | 21 GPa |
| Substrate beam thinnest thickness $h_0$ | 0.0005 m | Piezoelectric permittivity ${\varepsilon_{33}}^T$ | 15.93 nF/m |
| Smoothness coefficient $\varepsilon$ | 20 | Piezoelectric constant $e_{31}$ | −12.54 C/m$^2$ |
| Power order $m$ | 2 | Inductance $L_d$ | 1.242 H |

and

$$H_{t2}=\begin{bmatrix} 0 & 0 & 0 & 0 & 0 & 0 \\ 0 & 0 & 0 & 0 & 0 & 0 \\ iE_sI_sk_1r_1e^{ik_1L_i} & iE_sI_sk_2r_2e^{ik_2L_i} & iE_sI_sk_3r_3e^{ik_3L_i} & iE_sI_sk_4r_4e^{ik_4L_i} & -dE_sA_s\gamma\cos(\gamma L_i) & dE_sA_s\gamma\sin(\gamma L_i) \\ G_sA_s(ik_1-r_1)e^{ik_1L_i} & G_sA_s(ik_2-r_2)e^{ik_2L_i} & G_sA_s(ik_3-r_3)e^{ik_3L_i} & G_sA_s(ik_4-r_4)e^{ik_4L_i} & 0 & 0 \\ 0 & 0 & 0 & 0 & 0 & 0 \\ 0 & 0 & 0 & 0 & E_sA_s\gamma\cos(\gamma L_i) & -E_sA_s\gamma\sin(\gamma L_i) \end{bmatrix}.$$

### 2.2. Band structure analysis

Considering the continuity condition between each unit cell, the total transfer matrix $T$ between $n$th and $(n+1)$th unit cell can be obtained:

$$T=K_{pl}^{-1}\left(H_p+G\right)\left(K_p+G\right)^{-1}H_{pl}K_{pl}^{-1}\left(H_{t1}T_t+H_{t2}T_tB^{-1}A\right)\left(K_{t1}+K_{t2}B^{-1}A\right)^{-1}H_{pl}, \tag{34}$$

Assuming the meta-beam is infinitely long, the Bloch's theorem interprets the structural periodicity as:

$$\psi_1^{n+1}=e^{iqL}\psi_1^n, \tag{35}$$

where $q$ is the wave number, and $L$ is the total length of a unit cell, i.e., $L=L_{ABH}+L_p$. A standard eigenvalue problem is formulated by comparing Eq. (34) and (35):

$$\left|T-e^{iqL}I\right|=0, \tag{36}$$

where $I$ is a $6\times 6$ identity matrix. The dispersion relationships in both longitudinal and transverse directions of the proposed meta-beam can be determined by solvind Eq. (36). In the real band structure, band gaps occur in blank areas with no real solutions.

### 2.3. Transmittance spectra investigation

As mentioned in Section 1, directly applying conventional TMM leads to a collapse in transmittance calculations as a result of successive multiplication. Therefore, to improve the stability, RTMM is applied to is applied to predict the transmittance of the proposed meta-beam with 6-unit cells ($n=6$). The relationship between modal coordinates in each unit cell can be rewritten as follows:

$$S_{o,n}=US_{I,n}+f_n, \tag{37}$$

$$U=\left(H_p+G\right)\left(K_p+G\right)^{-1}H_{pl}K_{pl}^{-1}\left(H_{t1}T_t+H_{t2}T_tB^{-1}A\right)\left(K_{t1}+K_{t2}B^{-1}A\right)^{-1}H_{pl}K_{pl}^{-1}. \tag{38}$$

In the above equation, the subscripts $I$ and $O$ represent the input and output of a unit cell, and $U$ represents the local transfer matrix in a unit cell. $f_i$ is the column array of the load function exerted on each unit cell. Then, Eq. (37) can be divided as a matrix form:

$$\begin{bmatrix} S_a \\ S_b \end{bmatrix}_{O,n}=\begin{bmatrix} U_{11} & U_{12} \\ U_{21} & U_{22} \end{bmatrix}\begin{bmatrix} S_a \\ S_b \end{bmatrix}_{I,n}+\begin{bmatrix} f_a \\ f_b \end{bmatrix}_n \tag{39}$$

where $S_{I,1}$ is a zero vector, representing the zero boundary conditions, and $U_{11}\sim U_{22}$ are the submatrices formed by rearranging the local transfer matrix $U$.

Introduce the following Raccati transformation to Eqs.(37) and (39)

$$S_{aI,n}=p_nS_{bI,n}+q_n, \tag{40}$$

where

$$\begin{cases} p_{n+1}=(U_{11}p_n+U_{12})(U_{21}p_n+U_{22})^{-1} \\ q_{n+1}=U_{11}q_n+f_{an}-p_{n+1}(U_{21}q_n+f_{bn}). \end{cases} \tag{41}$$

$p_n$ and $q_n$ are recursive equations with the initial value $p_1=\begin{bmatrix} 0 & 0 & 0 \\ 0 & 0 & 0 \\ 0 & 0 & 0 \end{bmatrix}$, $q_1=\begin{bmatrix} 0 \\ 0 \\ 0 \end{bmatrix}$. The input and output state vectors of each component can thus be obtained through recursive relations and boundary conditions. By using RTMM, the number of matrix dimensions involved in the calculation can be reduced by half.

The transmittance is defined as the ratio of the output to the input, i.e., the magnitude ratio of the response displacement to the excitation displacement:

$$\tau=20\log_{10}(|W_n/W_0|). \tag{42}$$

which is often expressed in the decibel scale. Theoretically, the band gap can be defined as the region where the transmittance of an undamped metamaterial is below 0 dB.

## 3. Results and discussion

In this section, the above theoretical model is validated by a corresponding FE simulation, established using the Structural Mechanics (Solid) module of the commercial software COMSOL Multiphysics. RTMM is compared to the conventional TMM, accompanied by a detailed analysis of the instability inherent in conventional TMM, followed by a parametric study on both geometric and electric factors.

### 3.1. Finite element verification

Table 1 lists the geometric and material parameters of the proposed meta-beam under investigation. As the previous section introduces, the tapered beam segment is discretized in the modelling. Thus, it is essential to investigate the impact of the smoothness of the thickness variation of the ABH segment first. For ABH beams, the local wave number $k$, founded on the thickness $h(x)$, can be represented as [30,41]:

$$k=\left(\frac{12\rho\pi^2\omega^2}{Eh^2(x)}\right)^{0.25}. \tag{43}$$

The smoothness condition for the variation in beam thickness requires that the spatial variation of the flexural wave number be much smaller over a distance on the order of the wavelength. Mathematically, this can be expressed as follows:

$$\frac{dk}{dx}\frac{1}{k}\ll k. \tag{44}$$

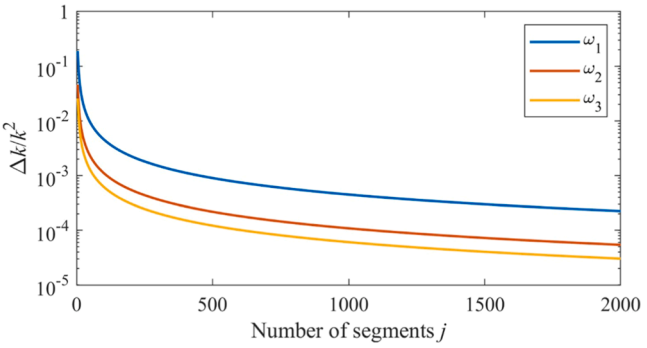


**Fig. 4.** $\Delta_k/k^2$ decreases with the increment of segment number $j$ at first three eigen frequencies of ABH segments.

The change in wavenumber between two adjacent segments with thickness of $h_2$ and $h_1$ can be calculated as:

$$\Delta k = \left(\frac{12\rho\pi^2\omega^2}{Eh_2^2}\right)^{0.25} - \left(\frac{12\rho\pi^2\omega^2}{Eh_1^2}\right)^{0.25}. \tag{45}$$

Since the thickness of ABH segments is governed by a power profile, it is reasonable to infer that the largest change in wavenumber occurs at the boundary where the plain segment transitions to the tapered segment. Thus, to meet the smoothness condition, a change in boundary should satisfy $\Delta k/k^2 \ll 1$. As shown in Fig. 4. the segment number $j$ is plotted versus $\Delta k/k^2$ at the first three eigen frequencies of the ABH segment $\omega_1$, $\omega_2$, and $\omega_3$. The result indicates that when the ABH segment is divided into >1000 sub-segments, the value of $\Delta k/k^2$ is significantly smaller than 1 at three natural frequencies. Therefore, discretizing the ABH segment into 1000 sub-segments fulfills the smoothness condition.

Fig. 5(a) shows the band structure of the proposed meta-beam with the specified parameters listed in Table 1. The dimensionless wavenumber along the $x$-axis is defined as $q^* = qL/\pi$. Fig. 6 presents the transmittance of the proposed meta-beam comprising 6 and 18 unit cells ($n = 6, 18$). As shown in Fig. 5(a) and Fig. 6, the theoretical results agree well with the FE simulation.

As shown in Fig. 5(a), the proposed meta-beam produces three band gaps, filled in light blue, covering the frequency ranges of [1082.5, 1100.3] Hz, [2153.3, 2332.1] Hz, and [6388.9, 10,446.1] Hz, respectively. In Fig. 5(b), the "stepped piezo" case refers to a configuration that includes piezoelectric elements but excludes the ABH structure, while the "double-leaf ABH" case features a purely ABH structure without any piezoelectric elements. They are provided as benchmarks to highlight the advantages of the proposed design that combines both features. It is important to note that all parameters used in the benchmark cases are identical to those in Fig. 5(a), ensuring a consistent basis for fair and meaningful comparison. The band gaps observed in the band structures of the stepped piezoelectric meta-beam and the double-leaf ABH beam are shaded in light green and yellow, respectively. While the first ([1083.0–1100.2] Hz) and second ([2187.1–2517.1] Hz) band gaps in the stepped piezoelectric meta-beam closely match those in the proposed meta-beam, its third band gap ([8972.7–9734.7] Hz) is notably narrower. Additionally, the two band gaps of the ABH beam span the frequency ranges of [1972.3, 2328.1] Hz and [6418.6, 9229.7] Hz. A comparative analysis with Fig. 5(b) reveals the formation mechanism for each band gap in the proposed meta-beam. The first band gap originates primarily from the piezoelectric effect. The second band gap emerges from the overlap between the second band gap of the stepped piezo-beam and the first band gap of the double-leaf ABH beam. Furthermore, the third band gap is significantly broadened due to the combined effect of the third band gap from the stepped piezoelectric beam and the second band gap from the double-leaf ABH beam, resulting in an even wider band gap in the integrated meta-beam. Overall, the proposed meta-beam combines the advantages of both designs: its total band gap width is increased by respectively 283.5 % and 34.3 % compared to the stepped piezoelectric meta-beam and double-leaf ABH beam.

It is worth noting that a band gap is theoretically defined as a region where the transmittance is below 0 dB. However, Fig. 6 shows additional regions that meet this theoretical requirement but cannot be considered as band gaps. Thus, the results from band structure analysis, as shaded in light blue, are essential as a reference for accurately identifying band gaps. Furthermore, the valley profile of the first band gap exhibits backward spikes, whereas those of the second and third band gaps remain smooth. This distinction suggests that the first band gap is induced by local resonance, while the third primarily arises from Bragg scattering mechanisms [77]. Fig. 6(a) demonstrates a computational collapse in the conventional TMM results at high frequencies. Furthermore, as shown in Fig. 6(b), a similar numerical instability occurs even in low-frequency domains when the number of unit cells increases.

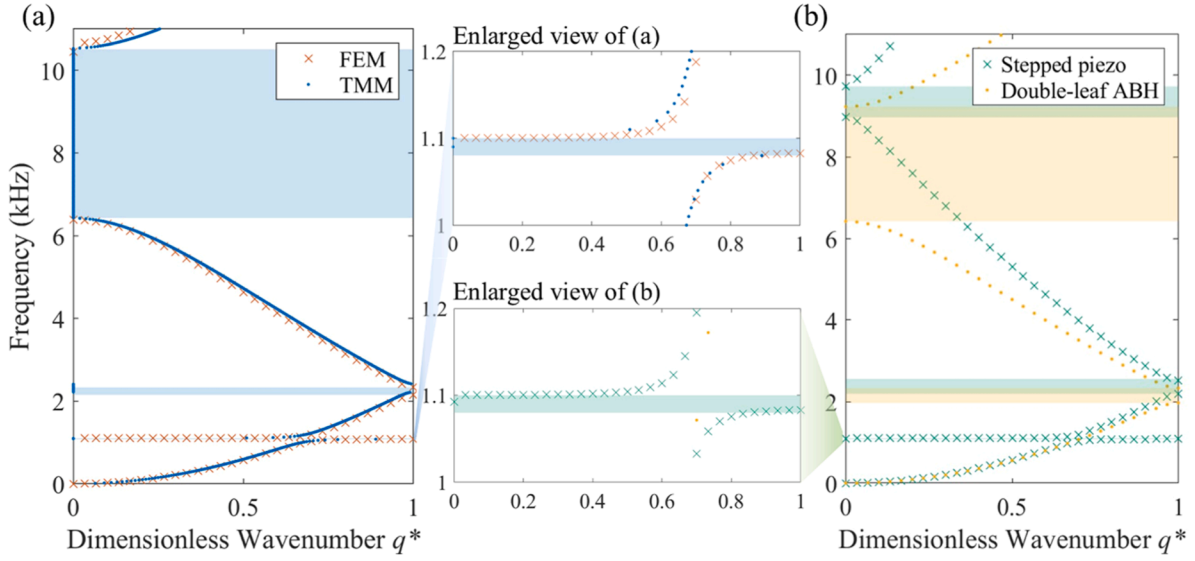


**Fig. 5.** Band structures of (a) proposed meta-beam with band gaps shaded in blue, (b) stepped piezoelectric meta-beam and double-leaf ABH beam with band gaps shaded in light green and yellow respectively. Total band gap width of proposed meta-beam is increased by respectively 283.5 % and 34.3 % compared to the stepped piezoelectric meta-beam and double-leaf ABH beam.

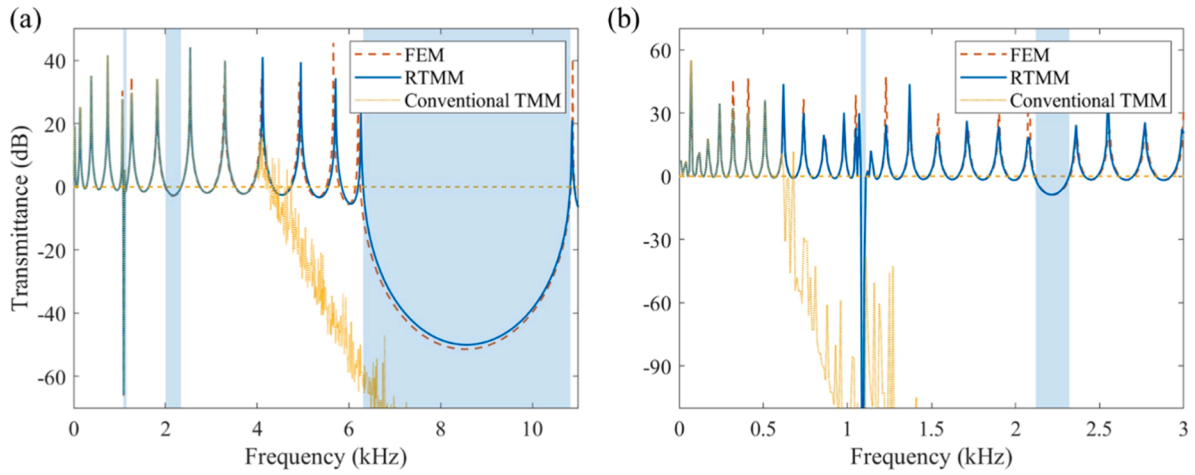


**Fig. 6.** Transmittance of proposed meta-beam with band gaps shaded in blue obtained using FEM, RTMM, and conventional TMM: (a) 6 unit cells, (b) 18 unit cells. Numerical failures can be found in high and low frequency domains respectively with conventional TMM.

Mathematically, the conventional TMM accumulatively multiplies local transfer matrices to produce a global transfer matrix, which is then applied with boundary conditions:

$$\begin{cases} \begin{bmatrix} T^{n-1} & -I \end{bmatrix} \begin{bmatrix} \psi_1 \\ \psi_n \end{bmatrix} = 0 \\ \begin{bmatrix} K_1 & 0 \\ 0 & H_n \end{bmatrix} \begin{bmatrix} \psi_1 \\ \psi_n \end{bmatrix} = \begin{bmatrix} \text{B.C.} \\ \text{B.C.} \end{bmatrix} \end{cases} \tag{46}$$

where B.C. represents the boundary conditions. Rewriting the Eq. (46), a $12 \times 12$ global transfer matrix $T^*$ can be obtained, in which elements with high magnitudes are located intensively.

This ill-conditioned matrix arises from either: (1) the direct multiplication of high-frequency components, or (2) the cumulative effect of successive multiplications of local transfer matrices. For instance, Fig. 7 (a) plots the heat map of $T^*$ at 8 kHz for the 6 unit cell meta-beam, where the failure had already begun. It is evident that the magnitudes of elements vary so remarkably that $T^*$ becomes ill-conditioned. As a reference, the change in the conditional number of $T^*$ is plotted in Fig. 7(b), in which the magnitude of the condition number keeps soaring up with the increase of frequency. Therefore, directly solving Eq. (46) using a basic algorithm becomes particularly challenging, especially in high-frequency domains or when dealing with structures containing a large number of unit cells.

In contrast, RTMM utilizes modal coordinates through a series of recursive equations rather than state coordinates as in conventional TMM. This approach significantly reduces the multiplication and, consequently, magnitudes of the matrix entries. Additionally, RTMM decomposes the transfer matrix into four sub-matrices, as shown in Eq. (39), storing zero elements in one of the sub-matrices in the first iteration. As a result, the disparity in magnitudes of the entries within each sub-matrix is reduced. Consequently, RTMM avoids the emergence of an ill-conditioned $T^*$, thereby improving the stability of the conventional TMM. Furthermore, compared to SEM, which is also a stable approach, RTMM offers superior computational efficiency. SEM constructs the global dynamic matrix by summating individual element matrices, a process that inherently increases the matrix dimension [28], particularly for complex metamaterials consisting of many unit cells. This matrix dimensional expansion significantly increases both computational time and memory consumption, posing challenges for large-scale systems. In contrast, RTMM preserves a constant matrix dimension by employing successive matrix multiplications, thereby reducing computational overhead and memory requirements. Additionally, by leveraging a recursive formulation presented in Eq. (41), RTMM further minimizes

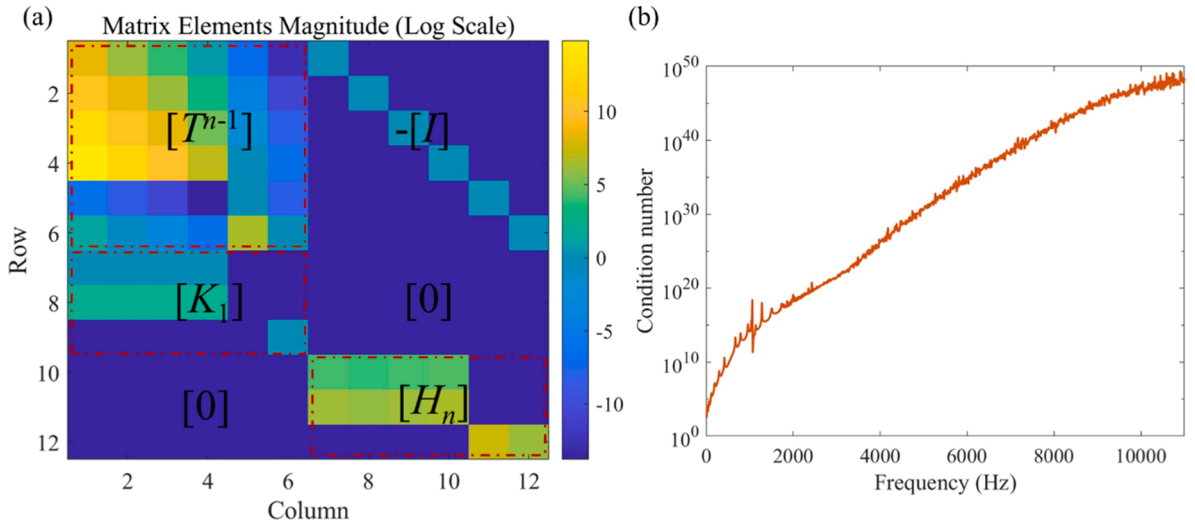


**Fig. 7.** Cause of failure in conventional TMM. (a) Heat map of an ill-conditioned global transfer matrix $T^*$ magnitude at 8 kHz. Color bars from blue to yellow represent magnitudes from small to large. (b) Rapid increase in condition number of $T^*$ with increment of frequency.

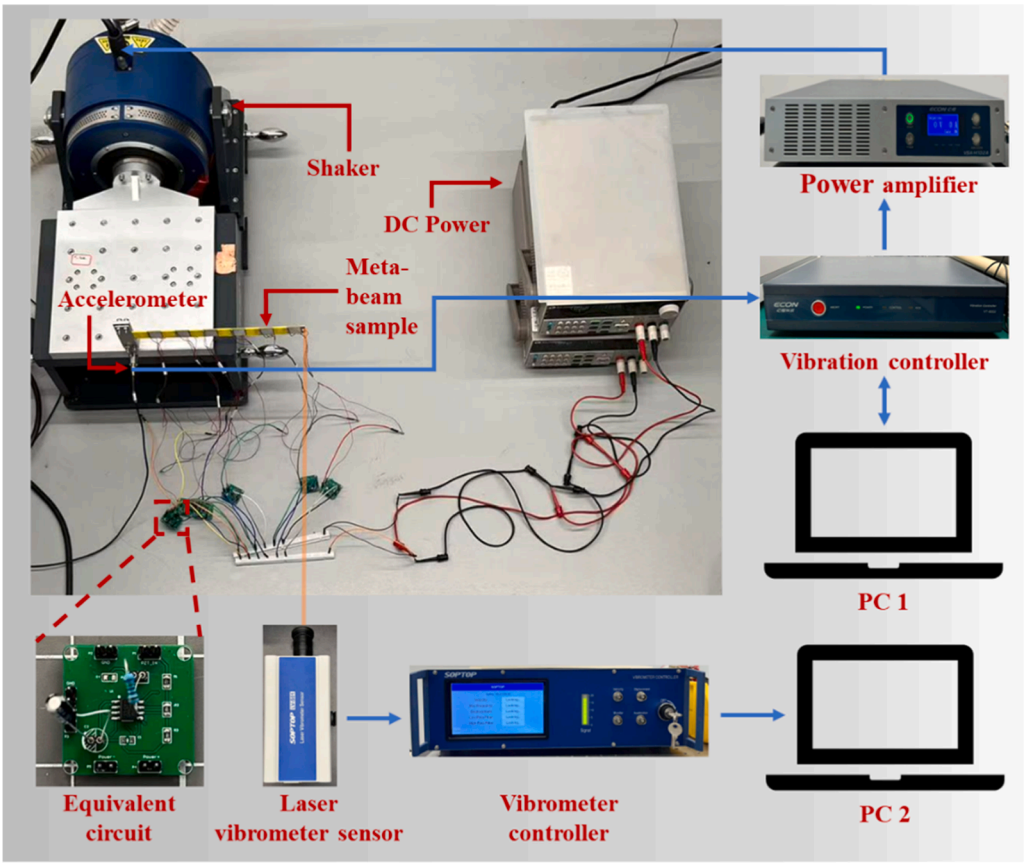


**Fig. 8.** Overview of experimental setup.

the computational resources needed. This efficiency advantage makes RTMM particularly well-suited for modeling metamaterials with a large number of unit cells, where the drawbacks of SEM become pronounced.

### 3.2. Experimental validation

To further validate the theoretical predictions derived from the RTMM method, a 6-unit-cell meta-beam prototype was fabricated using 3D printing and then experimentally tested. Polylactic Acid (PLA) was selected as the printing material due to its printability and cost-effectiveness. To accommodate manufacturing constraints, the physical prototype dimensions were optimized as follows: $L_{ABH} = 0.02$ m, $L_p = 0.0215$ m, $b = 0.02$ m, $L_t = 0.01$ m, $h_0 = 0.0006$ m, $h_p = 0.0002$ m, and $h_s = 0.002$ m. The PLA substrate has a Young's modulus $E_s$ of 3.15 GPa, shear modulus $G_s$ of 1.17 GPa, and a density $\rho_s$ of 1240 kg/m$^3$. For the piezoelectric material, PZT-5H was used for its superior performance

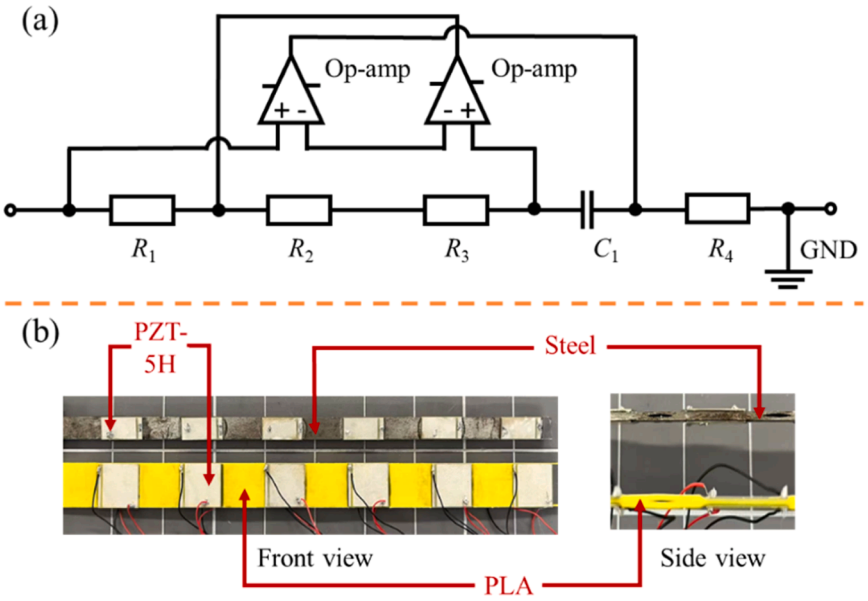


**Fig. 9.** (a) Diagram of Antoniou's synthetic inductor circuit, and (b) Proposed meta-beam samples fabricated using spring steel and PLA substrate.

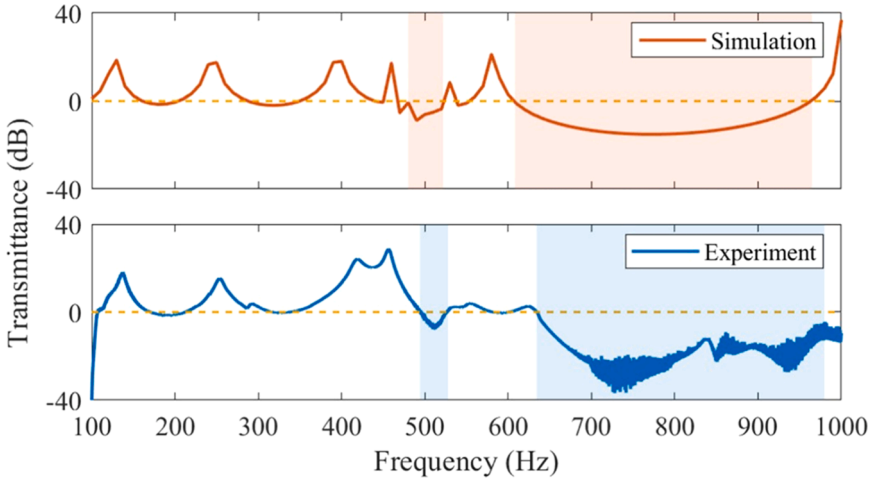


**Fig. 10.** Transmittance obtained by theoretical simulation and experiment with band gaps shaded in red and blue respectively.

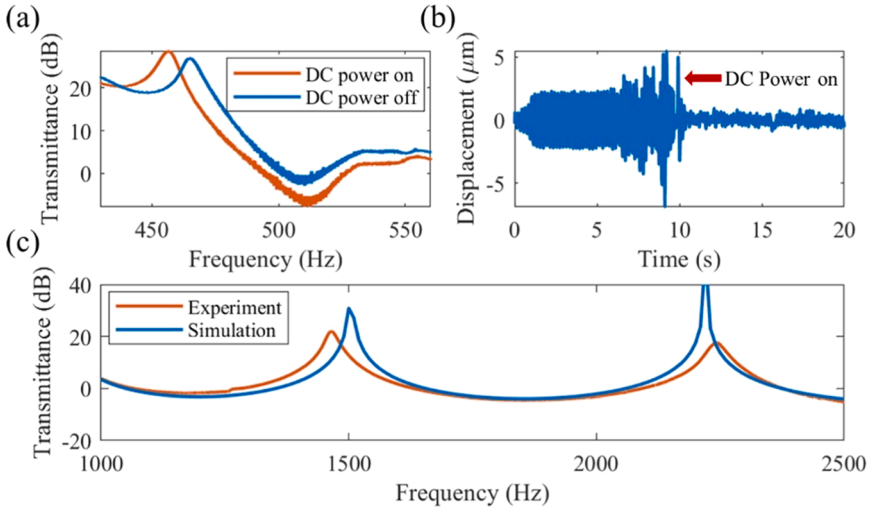


**Fig. 11.** Experimental verification: (a) Comparison of measured transmittance around the first band gap, where transmittance drops with active state. (b) Measured displacement decreases significantly after DC power supplement. (c) Transmittance of spring steel fabricated meta-beam obtained by theoretical simulation and experiment.

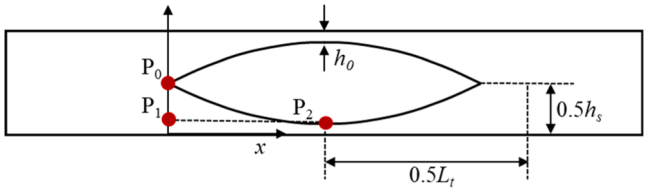


**Fig. 12.** Schematic of Bezier thickness profile governed tapered segment with a local coordinate system and three control points.

and availability, with material properties of $C_{11}^{E} = 60$ GPa, $C_{55}^{S} = 23$ GPa, and $\rho_p = 7500$ kg/m$^3$. The thickness profile follows a power-law distribution defined by smoothness coefficient $\varepsilon = 16$ and $m = 2$. The equivalent inductor $L_d$ is set to be 1 H, which is determined by

$$L_d = \frac{R_1 R_3 R_4 C_1}{R_2}. \tag{47}$$

The experimental configuration is illustrated in Fig. 8. Harmonic vibrations spanning 100–1000 Hz were generated using Econ VCS software, with a vibration controller (Econ. VT-9002) transmitting user-defined signals to a shaker (Econ. EDS) via a power amplifier (Econ. VSA-H102A). Displacement responses at the beam's free end were measured and recorded using a laser Doppler vibrometer (Soptop. LV-S01) synchronized to a dedicated controller. Notably, Antoniou's synthetic inductor circuit [78], as shown in Fig. 9(a), was integrated into the setup with a DC power supply to mitigate parasitic resistance effects, thereby preserving the fidelity of the l-C resonance [79]. Fig. 9(b) shows the two proposed meta-beams with spring steel and PLA as the substrate material. Transmittance was calculated using Eq. (42).

Experimental measurements identified two prominent band gaps: 494–528 Hz (attributed to LR effect) and 634–980 Hz (associated with BS effect), as shown in Fig. 10. These measured ranges exhibit slight upward shifts compared to theoretical predictions (480–522 Hz and 608–965 Hz). The geometric deviation is one of the key factors contributing to the above discrepancy. Manufacturing tolerances inherent in 3D printing and adhesive bonding processes introduce thickness variations, which alter bending stiffness and, as a result, perturb band gap positions.

Fig. 11(a) demonstrates the transmittance contrast between the active (DC-powered) and passive (short-circuit) configurations. Activating the synthetic inductor circuit via DC power reduces transmittance from –0.87 dB to –7.80 dB, confirming enhanced *l-C* resonance efficacy in creating a deep band gap. In addition, Fig. 11(b) shows a fivefold

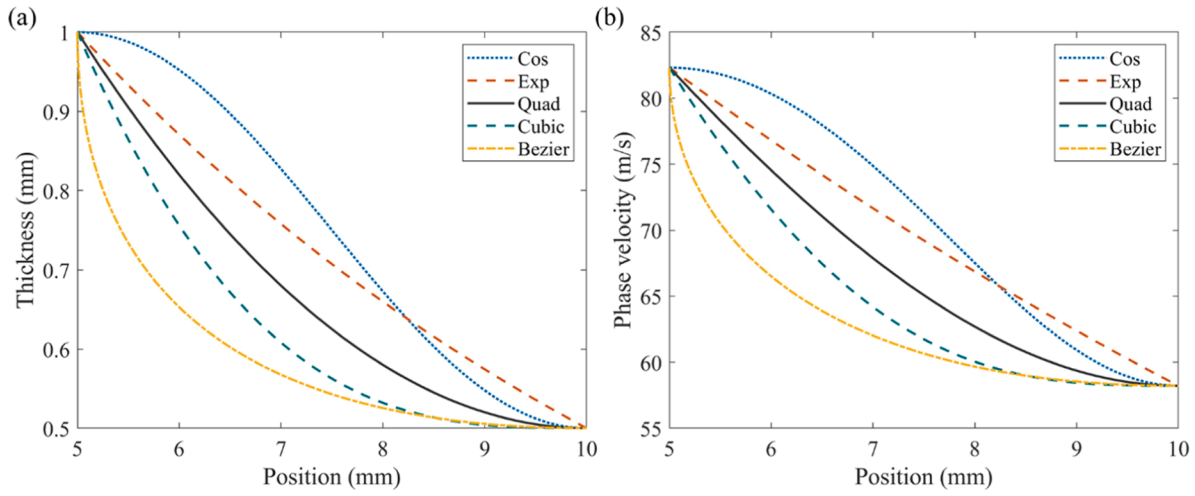


**Fig. 13.** Properties of cosine, exponential, quadratic power law, cubic power law, and Bezier thickness profiles. (a) Thickness $h_t$ at tapered segment. (b) Phase velocity $c_{ph}$ along tapered segment at 8 kHz.

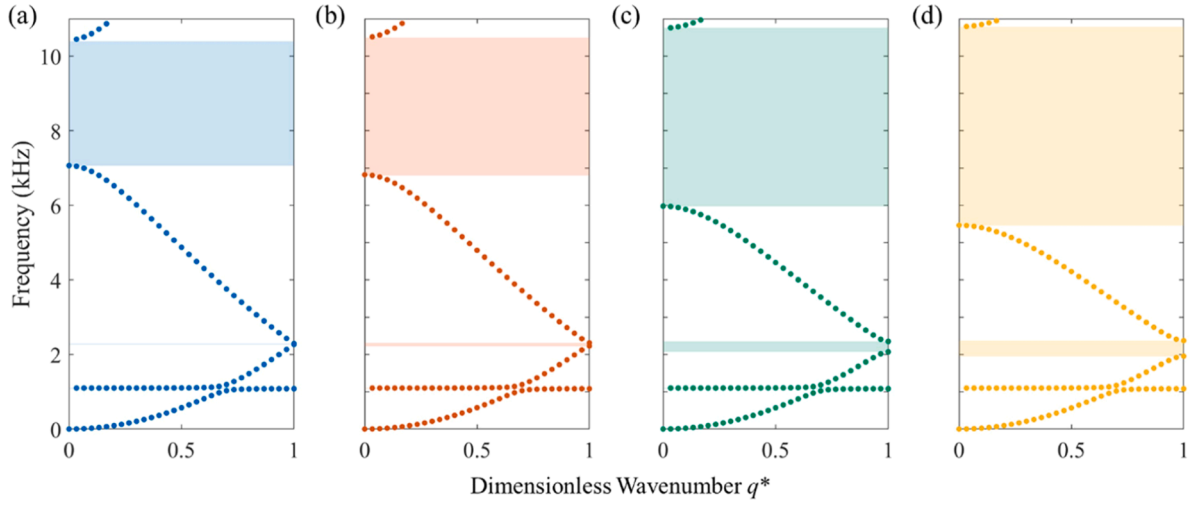


**Fig. 14.** Band structures with (a) cosine, (b) exponential, (c) cubic power law, and (d) Bezier thickness profiles with band gaps shaded in blue, red, green and yellow respectively.

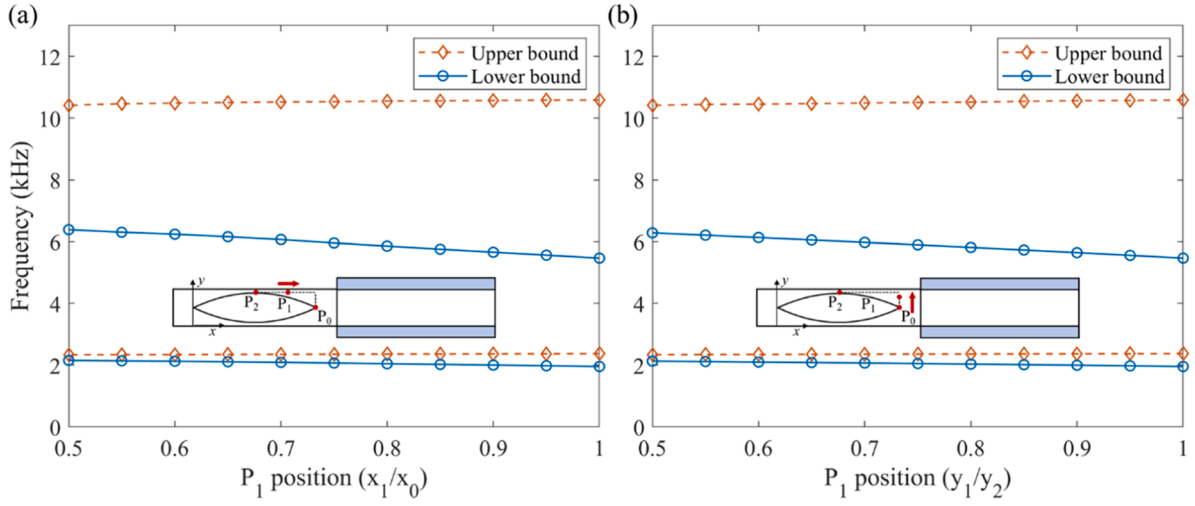


**Fig. 15.** Effect of control point $P_1$ on band gaps. $P_1$ moves (a) horizontally, and (b) vertically. Second band gap tends to broaden with $P_1$ moving towards corner.

displacement reduction (from 5 μm to 1 μm) at 511 Hz (the deepest valley of the first band gap) after DC power is applied, demonstrating the profound efficiency in vibration suppression.

The discrepancy in the high-frequency domain is noteworthy, as the experimental transmittance consistently appears lower than the theoretical prediction. Additionally, signal contamination from parasitic vibrations introduces noise, obscuring the expected smooth transmittance valley. These issues are primarily attributed to the pronounced damping effect in the high-frequency domain [80]. For instance, around 900 Hz, an unexpected resonant peak appears with a transmittance value below 0 dB. According to fundamental principles of vibration and dynamics, resonance typically results in significant structural vibrations, often yielding transmittance values well above 0 dB. The fact that this peak remains below 0 dB indicates an exceptionally high damping effect within the system. To address these limitations, a spring steel meta-beam sample, depicted in Fig. 9(b), was tested across an extended range of 1000–2500 Hz. As shown in Fig. 11(c), this configuration achieves improved coherence between experimental and simulated results, without the noise induced by the material damping. The enhanced agreement validates the efficiency of RTMM in predicting the band gap for the proposed meta-beam.

### 3.3. Parametric study

Based on the theoretical model established, the influences of the thickness profile and electric parameters are thoroughly investigated. The default geometric and material parameters are the same as those in Table 1.

#### 3.3.1. Influence of thickness profile

As introduced in earlier sections, the thickness of the ABH indentation is conventionally governed by the power law profile, $h_t(x) = h_s - 2(\varepsilon x^m + h_0)$. In addition to the power law, other thickness profiles that taper to approximately zero thickness at the edge of a segment can also produce a similar ABH effect. While higher-order power law, exponential, and cosine profiles have been discussed and compared in terms of energy dissipation and wave reflection [81], this paper investigates the influences of these profiles and the Bezier thickness profile on the band gap phenomenon. The formula of the Bezier profile in each tapered segment can be written as:

$$\begin{cases} x(t) = (1-t^2)x_0 + 2t(1-t)x_1 + t^2 x_2 \\ y(t) = (1-t^2)y_0 + 2t(1-t)y_1 + t^2 y_2 \end{cases}, t \in [0,1] \tag{48}$$

where $P_0$ ($x_0$, $y_0$), $P_1$ ($x_1$, $y_1$), and $P_2$ ($x_2$, $y_2$) are the three control points of each tapered segment, as shown in Fig. 12.

It is worth noting that the length of the tapered segment $L_t$, the thickness at the junction, and the truncated edge remain constant across all the profiles, as plotted in Fig. 13(a). To further study the influences of different thickness profiles, the change in phase velocity at 8 kHz is shown in Fig. 13(b). Using local wave number $k$ obtained by Eq. (43), the phase velocity $c_{ph}$ is defined as:

$$c_{ph} = \frac{\omega\pi}{k}. \tag{49}$$

As depicted in Fig. 13, the phase velocities of the wave in both profiles decrease as the thickness decreases, indicating that most of the energy dissipation occurs at the thinnest point, where the wave is concentrated. From an energy perspective, since the phase velocity of the Bezier profile, shown in Fig. 13(b), is consistently smaller than that of the other profiles, it is reasonable to deduce that the energy dissipation in the Bezier profile is greater than in other profiles before reaching the thinnest point. Consequently, the Bezier profile may produce a wider band gap in the band structure.

To validate the aforementioned deduction, the band structures for different thickness profiles are plotted in Fig. 14. It is evident that the second and third band gaps are sensitive to changes in thickness profiles. The widths of the band gaps are correlated with the phase velocities. Specifically, profiles with higher phase velocities lead to narrower band gaps, as shown in Fig. 14(a) and (b), while those with lower phase velocities result in broader band gaps, as depicted in Fig. 14(c) and (d). Notably, the Bezier profile, which exhibits the lowest phase velocity in Fig. 13(b), produces the broadest second and third band gaps, as illustrated in Fig. 14(d).

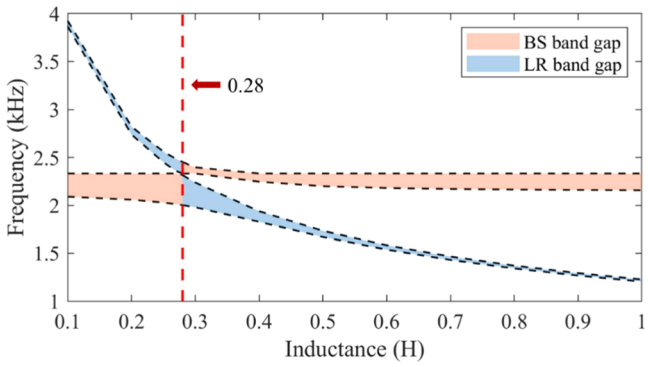


**Fig. 16.** Influence of inductance on band gap formation, with critical inductance of 0.28 H for band gap coupling.

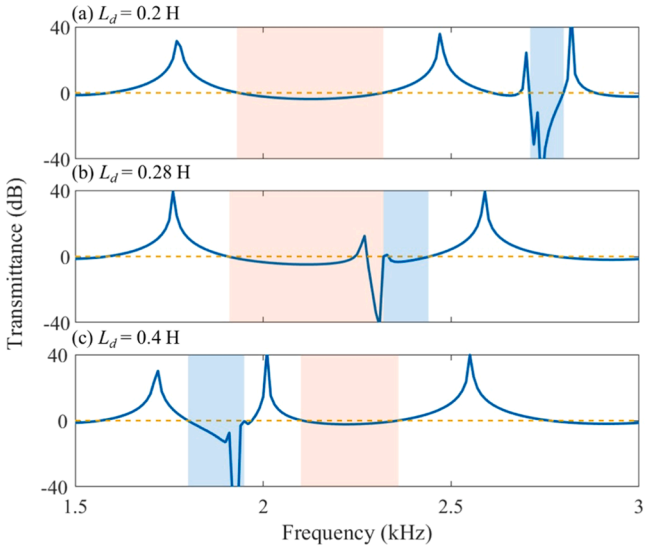


**Fig. 17.** Transmittance of meta-beam with LR and BS band gaps shaded in pink and blue, respectively. (a) $L_d$ = 0.2 H, (b) $L_d$ = 0.28 H, (c) $L_d$ = 0.4 H LR and BS band gaps merge as a wider band gap at inductance of 0.28 H.

Furthermore, Fig. 15 unveils the impact of control points on the formation of the second and third band gaps. Since the first band gap is insensitive to the changes in thickness profiles, it is not discussed here. Control points $P_0$ and $P_2$ are fixed to maintain the initial and terminal thickness, as well as the length of the indentation. As the free point $P_1$ shifts horizontally and vertically, as depicted in Fig. 15(a) and (b), both the second and third band gaps attain their broadest when $P_1$ is positioned at the terminals. This movement towards the terminals lowers the thickness profile, as shown in Fig. 13(a), with a corresponding decrease in phase velocity in Fig. 13(b). The influences of the free control point on band gaps further support the earlier conclusion that a lower phase velocity leads to a wider band gap.

#### 3.3.2. Influence of electric parameters

As depicted in Fig. 6, the valley profile of the first band gap features a sharp spike, while those of the second and third band gaps are smooth.

From this, we can deduce that the first band gap is primarily due to local resonance, and the second and third band gaps are attributed to Bragg scattering [77]. To explore the possibility of merging the LR and BS band gaps into a wide, combined band gap, the influence of the inductance on the band gap formation is prioritized. As illustrated in Fig. 16, the LR and BS band gaps, shaded in pink and blue, approach and separate from each other as the inductance varies. Notably, at an inductance of 0.28 H, the two band gaps converge to form a combined band gap.

In addition, Fig. 17 compares the transmittance of a 6-unit meta-beam with the critical inductance of 0.28 H and two adjacent inductances, 0.2 and 0.4 H The suppression regions induced by LR and BS effects, are shaded in pink and blue, respectively. As depicted in Fig. 17 (b), while there is a peak, the two band gaps remain distinguishable by referencing Fig. 16, overlapping to form a wider, combined suppression region. The suppression region ranges are [1934.3, 2318.9] Hz and [2706.5, 2799.0] Hz in Fig. 17(a), and [1800.0, 1949.6] Hz and [2105.2, 2358.1] Hz in Fig. 17(c). Compared to the total bandwidth of the discrete suppression regions of meta-beam with inductances of 0.2 H and 0.4 H, the overlapped suppression region, ranging from 1906.6 Hz to 2443.0 Hz, is increased by 12.4 % and 33.2 %, respectively.

## 4. Conclusions

This study has demonstrated that integrating double-leaf ABH configurations with adaptive piezoelectric shunting circuits enables ultra-broadband vibration suppression through synergistic physical mechanisms. The proposed meta-beam effectively combines piezoelectric and ABH effects, resulting in the formation of three wide band gaps. To address the computational limitations of conventional TMM in high-frequency domains, a theoretical model was developed using the RTMM. The accuracy of the model was validated against an FE model. Furthermore, an experimental study was conducted to further validate the proposed meta-beam, using an equivalent circuit to emulate inductive components.

Compared to conventional piezoelectric and ABH meta-beams, the proposed meta-beam achieves a 283.5 % and 34.2 % wider total band gap range respectively. In addition, the effects of ABH indentation thickness profiles on band gap formation were investigated, along with a discussion from the energy perspective. Among various profiles, the Bezier profile was notable for inducing the widest band gap. Furthermore, the tunability of the meta-beam was explored through a parametric study on inductance, where a wider unified suppression region was realized by merging the LR and BS band gaps through inductance tuning.

Overall, this study presents a new paradigm for metamaterial design by seamlessly integrating multi-physics coupling strategies, surpassing the limitations of single mechanism approaches. The demonstrated vibration control capabilities make this meta-beam design a highly promising solution for broadband and tunable vibration suppression.

## CRediT authorship contribution statement

**Jiazhen Zhang:** Writing – original draft, Validation, Software, Methodology, Investigation, Conceptualization. **Guobiao Hu:** Writing – review & editing, Supervision, Funding acquisition, Conceptualization. **Hao Tang:** Validation. **Yaowen Yang:** Writing – review & editing, Supervision, Conceptualization.

## Declaration of competing interest

The authors declare that they have no known competing financial interests or personal relationships that could have appeared to influence the work reported in this paper.

## Acknowledgments

This work was financially supported by the State Key Laboratory of Structural Analysis for Industrial Equipment, Dalian University of Technology, China (S22311), the National Natural Science Foundation of China (Grant No.: 52305135), the Guangdong Provincial Project (Grant No 2023QN10L545), and the Guangzhou Municipal Science and Technology Bureau (Grant Nos. SL2023A03J00869, SL2023A04J01741).

## Data availability

Data will be made available on request.

## References

[1] Sigalas MM. Elastic and acoustic wave band structure. J. Sound. Vib. 1992;158:377–82.
[2] Kushwaha MS, Halevi P, Dobrzynski L, Djafari-Rouhani B. Acoustic band structure of periodic elastic composites. Phys. Rev. Lett. 1993;71:2022–5.
[3] Kushwaha MS, Halevi P, Martínez G, Dobrzynski L, Djafari-Rouhani B. Theory of acoustic band structure of periodic elastic composites. Phys. Rev. B 1994;49:2313–22.
[4] Ruzzene M, Baz A. Control of wave propagation in periodic composite rods using shape memory inserts. J. Vib. Acoust. 1999;122:151–9.
[5] Oudich M, Senesi M, Assouar MB, Ruzenne M, Sun J-H, Vincent B, Hou Z, Wu T-T. Experimental evidence of locally resonant sonic band gap in two-dimensional phononic stubbed plates. Phys. Rev. B 2011;84:165136.
[6] Raghavan L, Phani AS. Local resonance bandgaps in periodic media: theory and experiment. J. Acoust. Soc. Am. 2013;134:1950–9.
[7] Deutsch IH, Spreeuw RJC, Rolston SL, Phillips WD. Photonic band gaps in optical lattices. Phys. Rev. A 1995;52:1394–410.
[8] Sutter-Widmer D, Deloudi S, Steurer W. Prediction of Bragg-scattering-induced band gaps in phononic quasicrystals. Phys. Rev. B 2007;75:094304.
[9] Liu Z, Zhang X, Mao Y, Zhu YY, Yang Z, Chan CT, Sheng P. Locally resonant sonic materials. Science (1979) 2000;289:1734–6.
[10] Xiao Y, Wang S, Li Y, Wen J. Closed-form bandgap design formulas for beam-type metastructures. Mech. Syst. Signal. Process. 2021;159:107777.
[11] Hu G, Tang L, Cui X. On the modelling of membrane-coupled Helmholtz resonator and its application in acoustic metamaterial system. Mech. Syst. Signal. Process. 2019;132:595–608.
[12] Thorp O, Ruzzene M, Baz A. Attenuation and localization of wave propagation in rods with periodic shunted piezoelectric patches. Smart Mater. Struct. 2001;10:979.
[13] Chen S, Wang G, Wen J, Wen X. Wave propagation and attenuation in plates with periodic arrays of shunted piezo-patches. J. Sound. Vib. 2013;332:1520–32.
[14] Sugino C, Ruzzene M, Erturk A. An analytical framework for locally resonant piezoelectric metamaterial plates. Int. J. Solids. Struct. 2020;182-183:281–94.
[15] Schimidt CS, de Oliveira LPR, De Marqui C. Vibro-acoustic performance of graded piezoelectric metamaterial plates. Compos. Struct. 2024;327:117656.
[16] Li Y, Liu Z, Zhou H, Yi K, Zhu R. Broadening bandgaps in a multi-resonant piezoelectric metamaterial plate via bandgap merging phenomena. Sci. Rep. 2024;14:16127.
[17] Jian Y, Tang L, Hu G, Li Z, Aw KC. Design of graded piezoelectric metamaterial beam with spatial variation of electrodes. Int. J. Mech. Sci. 2022;218:107068.
[18] Jian Y, Hu G, Tang L, Shen Y, Zhan Y, Aw K. Adaptive piezoelectric metamaterial beam: autonomous attenuation zone adjustment in complex vibration environments. Smart Mater. Struct. 2023;32:105023.
[19] Lin L-F, Lu Z-Q, Zhao L, Zheng Y-S, Ding H, Chen L-Q. Vibration isolation of mechatronic metamaterial beam with resonant piezoelectric shunting. Int. J. Mech. Sci. 2023;254:108448.
[20] Liu Y, Chunyu H, Liu D. Broadband vibration suppression of graded/disorder piezoelectric metamaterials. Mechan. Adv. Mater. Struct. 2023;30:710–23.
[21] Hu G, Xu J, Tang L, Lan C, Das R. Tunable metamaterial beam using negative capacitor for local resonators coupling. J. Intell. Mater. Syst. Struct. 2020;31:389–407.
[22] Yi K, Collet M. Broadening low-frequency bandgaps in locally resonant piezoelectric metamaterials by negative capacitance. J. Sound. Vib. 2021;493:115837.
[23] Zheng Y, Yuan H, Feng W, Qu Y, Luo Y. Enhancing sound transmission loss of a piezoelectric metastructure shell in the low-frequency range using negative-capacitance shunting. Europ. J. Mechan. - A/Solids 2025;111:105554.
[24] Bao B, Lallart M, Guyomar D. Manipulating elastic waves through piezoelectric metamaterial with nonlinear electrical switched dual-connected topologies. Int. J. Mech. Sci. 2020;172:105423.
[25] Xia D, Pu X, Tong S, Xu J. Piezoelectric metamaterial with digitally controlled nonlinear shunt circuit for broadband wave attenuation. Appl. Phys. Lett. 2024;124.
[26] Chen B, Zheng Y, Dai S, Qu Y. Bandgap enhancement of a piezoelectric metamaterial beam shunted with circuits incorporating fractional and cubic nonlinearities. Mech. Syst. Signal. Process. 2024;212:111262.
[27] Li S, Xu J, Tang J. Adaptive acoustic metamaterial with periodic piezoelectric network. SPIE 2017.

[28] Hu G, Tang L, Yang Y, Yu D, Zi Y. High-fidelity dynamics of piezoelectric covered metamaterial Timoshenko beams using the spectral element method. Smart Mater. Struct. 2023;32:095023.
[29] Nair G, Pilllai MA. Parametric optimization of stepped piezoelectric cantilever beam for vibration energy harvesting. In: 2024 IEEE International Conference on Electronics, Computing and Communication Technologies (CONECCT); 2024. p. 1–4.
[30] Krylov VV, Tilman FJBS. Acoustic 'black holes' for flexural waves as effective vibration dampers. J. Sound. Vib. 2004;274:605–19.
[31] Pekeris CL. Theory of propagation of sound in a half-space of variable sound velocity under conditions of formation of a shadow zone. J. Acoust. Soc. Am. 1946; 18:295–315.
[32] Mironov M. Propagation of a flexural wave in a plate whose thickness decreases smoothly to zero in a finite interval. Sov. Phys. Acoust. 1988;34:318–9.
[33] Tang L, Cheng L. Broadband locally resonant band gaps in periodic beam structures with embedded acoustic black holes. J. Appl. Phys. 2017:121.
[34] Gao W, Qin Z, Chu F. Broadband vibration suppression of rainbow metamaterials with acoustic black hole. Int. J. Mech. Sci. 2022;228:107485.
[35] He C, Zhang F, Lim KM, Jiang J, Zhao J. Wave attenuation of a laminated acoustic black hole array in a load-bearing beam structure. Thin-Walled Struct. 2023;188: 110821.
[36] Yao B, Zhang Y, Zhou Q, He B, Wang G, Rui X. Vibration isolator using graded reinforced double-leaf acoustic black holes - theory and experiment. J. Sound. Vib. 2024;570:118003.
[37] Gao N, Wei Z, Hou H, Krushynska AO. Design and experimental investigation of V-folded beams with acoustic black hole indentations. J. Acoust. Soc. Am. 2019;145: EL79–83.
[38] Deng J, Gao N, Chen X. Ultrawide attenuation bands in gradient metabeams with acoustic black hole pillars. Thin-Walled Struct. 2023;184:110459.
[39] Zhao L, Liu Y, Liao B, Liu F, Sun Z. Resonant-pillar-type acoustic black hole for ultralow-frequency vibration reduction. Europhys. Lett. 2024;146:30003.
[40] Deng J, Guasch O. On the bandgap mechanism of periodic acoustic black holes. J. Sound. Vib. 2024;579:118379.
[41] Yu Y, Jia X-x, Ouyang H, Du Y, Peng Y. Dynamic properties investigation of an acoustic black hole beam with dynamic vibration absorber based on analytical method. J. Sound. Vib. 2024;570:118053.
[42] Chen X, Zhao J, Deng J, Jing Y, Pu H, Luo J. Low-frequency enhancement of acoustic black holes via negative stiffness supporting. Int. J. Mech. Sci. 2023;241: 107921.
[43] Ji H, Han B, Cheng L, Inman DJ, Qiu J. Frequency attenuation band with low vibration transmission in a finite-size plate strip embedded with 2D acoustic black holes. Mech. Syst. Signal. Process. 2022;163:108149.
[44] Tang L, Cheng L. Ultrawide band gaps in beams with double-leaf acoustic black hole indentations. J. Acoust. Soc. Am. 2017;142:2802–7.
[45] TARGOFF WP. The associated matrices of bending and coupled bending-torsion vibrations. J. Aeronaut. Sci. 1947;14:579–82.
[46] Banerjee A. Non-dimensional analysis of the elastic beam having periodic linear spring mass resonators. Meccanica 2020;55:1181–91.
[47] E L, Wu Z, Li F, Zou G. A finite/spectral element hybrid method for modeling and band-gap characterization of metamaterial sandwich plates. Materials. (Basel) 2023;16:1098.
[48] Nobrega ED, Gautier F, Pelat A, Dos Santos JMC. Vibration band gaps for elastic metamaterial rods using wave finite element method. Mech. Syst. Signal. Process. 2016;79:192–202.
[49] Xie L, Xia B, Liu J, Huang G, Lei J. An improved fast plane wave expansion method for topology optimization of phononic crystals. Int. J. Mech. Sci. 2017;120:171–81.
[50] Shen Y, Lacarbonara W. Nonlinear plane-wave expansion method for analyzing dispersion properties of piezoelectric metamaterial lattices with encapsulated resonators. Nonlinear. Dyn. 2024.
[51] Wu X, Li Q, Qin S, Shao J, Jin C, Guan H. Theoretical, numerical, and experimental study on the sound insulation performance of membrane-type acoustic metamaterial under general constraints. J. Vibr. Eng. Technol. 2025;13:74.
[52] Li X, Ding Q. Sound radiation of a beam with a wedge-shaped edge embedding acoustic black hole feature. J. Sound. Vib. 2019;439:287–99.
[53] Yao B, Zhang Y, Zhou Q, He B, Rui X. Vibration isolation by a periodic beam with embedded acoustic black holes based on a hybrid dynamics method. J. Low Freq. Noise, Vibrat. Active Control 2023;42:1419–33.
[54] Lin Z, Al Ba'ba'a H, Tol S. Piezoelectric metastructures for simultaneous broadband energy harvesting and vibration suppression of traveling waves. Smart Mater. Struct. 2021;30:075037.
[55] Horner GC, Pilkey WD. The Riccati Transfer Matrix method. J. Mechan. Design 1978;100:297–302.
[56] He B, Rui X, Wang G. Riccati discrete time transfer matrix method for elastic beam undergoing large overall motion. Multibody Syst. Dyn. 2007;18:579–98.
[57] Wang J, Rui X, He B, Wang X, Zhang J, Xie K. Transfer matrix method for the analysis of multiple natural frequencies. Mathematics 2024;12:1413.
[58] Wei P-F, He M-X, Ding Q. Vibration and sound radiation of acoustic black hole beams on Pasternak foundation by the Riccati transfer matrix method. Appl. Acoust. 2024;217:109840.
[59] Gu JJ, Rui XT, Zhang JS. Riccati transfer matrix method for linear multibody systems with closed loops. AIP. Adv. 2020;10.
[60] Deng J, Guasch O, Zheng L, Song T, Cao Y. Semi-analytical model of an acoustic black hole piezoelectric bimorph cantilever for energy harvesting. J. Sound. Vib. 2021;494:115790.
[61] Li H, Doaré O, Touzé C, Pelat A, Gautier F. Energy harvesting efficiency of unimorph piezoelectric acoustic black hole cantilever shunted by resistive and inductive circuits. Int. J. Solids. Struct. 2022;238:111409.
[62] Ji H, Liang Y, Qiu J, Cheng L, Wu Y. Enhancement of vibration based energy harvesting using compound acoustic black holes. Mech. Syst. Signal. Process. 2019; 132:441–56.
[63] Xie M, Gao F, Zhang P, Wei Y, Tong M, He Y, Yan G. Study on the influence factors on harvesting capacity of a piezoelectric vibration energy harvesting system covered on curved beam with acoustic black hole. Shock Vibrat. 2023;2023: 6604388.
[64] Du W, Xiang Z, Qiu X. Stochastic analysis of an acoustic black hole piezoelectric energy harvester under gaussian white noise excitation. Appl. Math. Model. 2024; 131:22–32.
[65] Zhang L, Kerschen G, Cheng L. Electromechanical coupling and energy conversion in a PZT-coated acoustic black hole beam. Int. J. Appl. Mech. 2020;12:2050095.
[66] Benjamin SB, Kenneth AC. Improved negative capacitance shunt damping with the use of acoustic black holes. Proc.SPIE 2014:90571Z.
[67] Zhao L. Passive vibration control based on embedded acoustic black holes. J. Vib. Acoust. 2016;138.
[68] Zhao L, Semperlotti F. Embedded acoustic black holes for semi-passive broadband vibration attenuation in thin-walled structures. J. Sound. Vib. 2017;388:42–52.
[69] Cheer J, Hook K, Daley S. Active feedforward control of flexural waves in an acoustic Black hole terminated beam. Smart Mater. Struct. 2021;30:035003.
[70] Wan Z, Zhu X, Li T, Nie R. Low-frequency multimode vibration suppression of an acoustic black hole beam by shunt damping. J. Vib. Acoust. 2022;144.
[71] Wan Z, Zhu X, Li T, Fu J. A method for improving wave suppression ability of acoustic black hole plate in low-frequency range. Thin-Walled Struct. 2023;182: 110327.
[72] Wang H, Ji H, Wu Y, Qiu J. Innovative hybrid approach for broadband vibration suppression: integrating semi-active piezoelectric shunt damping and passive acoustic black hole effect. J. Intell. Mater. Syst. Struct. 2025 1045389X251315214.
[73] Zhang L, Kerschen G, Cheng L. Nonlinear features and energy transfer in an acoustic Black hole beam through intentional electromechanical coupling. Mech. Syst. Signal. Process. 2022;177:109244.
[74] Zhang L, Sun X, Dietrich J, Kerschen G, Cheng L. Enhanced energy transfer and multimodal vibration mitigation in an electromechanical acoustic black hole beam. J. Sound. Vib. 2023;561:117841.
[75] Chen X, Jing Y, Zhao J, Deng J, Cao X, Pu H, Cao H, Huang X, Luo J. Tunable shunting periodic acoustic black holes for low-frequency and broadband vibration suppression. J. Sound. Vib. 2024;580:118384.
[76] Wu W, Shan X, Zhang H, Sun C, Wang J, Sui G, Jiang T. Implementing the inverse design and vibration isolation applications of piezoelectric acoustic black hole beams by machine learning. Thin-Walled Struct. 2025;211:113074.
[77] Yu D, Hu G, Ding W, Yang Y, Hong J. Zero-thermal-expansion metamaterial with broadband vibration suppression. Int. J. Mech. Sci. 2023;258:108590.
[78] Wang G, Chen S, Wen J. Low-frequency locally resonant band gaps induced by arrays of resonant shunts with Antoniou's circuit: experimental investigation on beams. Smart Mater. Struct. 2011;20:015026.
[79] Jian Y, Hu G, Tang L, Tang W, Abdi M, Aw KC. Analytical and experimental study of a metamaterial beam with grading piezoelectric transducers for vibration attenuation band widening. Eng. Struct. 2023;275:115091.
[80] Zhang J, Peng X, Yu D, Hu G, Yang Y. Rigid-elastic combined metamaterial beam with tunable band gaps for broadband vibration suppression. J. Vib. Acoust. 2024; 146.
[81] Karlos A, Elliott SJ, Cheer J. Higher-order WKB analysis of reflection from tapered elastic wedges. J. Sound. Vib. 2019;449:368–88.